30 μm thick GaAs X-ray p$^+$-i-n$^+$ photodiode grown by MBE

G. Lioliou[1,a)], C. L. Poyser[2], S. Butera[1], R. P. Campion[2], A. J. Kent[2], A. M. Barnett[1]

[1]Space Research Group, Sch. of Engineering and Informatics, University of Sussex, Falmer, Brighton, BN1 9QT, UK
[2]School of Physics and Astronomy, University of Nottingham, Nottingham NG7 2RD, UK

Abstract

A GaAs p$^+$-i-n$^+$ photodiode detector with a 30 μm thick i layer and a 400 μm diameter was processed using standard wet chemical etching from material grown by molecular beam epitaxy. The detector was characterized for its electrical and photon counting X-ray spectroscopic performance at temperatures from 60 °C to -20 °C. The leakage current of the detector decreased from 1.247 nA ± 0.005 nA (= 0.992 μA/cm^2 ± 0.004 μA/cm2) at 60 °C to 16.0 pA ± 0.5 pA (= 12.8 nA/cm2 ± 0.4 nA/cm2) at -20 °C, at the maximum investigated applied reverse bias, -100 V (corresponding to an applied electric field of 33 kV/cm). An almost uniform effective carrier concentration of 7.1×10^{14} cm^{-3} ± 0.7×10^{14} cm^{-3} was found at distances between 1.7 μm and 14 μm below the p$^+$-i junction, which limited the depletion width to 14 μm ± 1 μm, at the maximum applied reverse bias (-100 V). Despite butterfly defects having formed during the epitaxial growth, ^{55}Fe X-ray spectra were successfully obtained with the detector coupled to a custom-made charge-sensitive preamplifier; the best energy resolution (Full Width at Half Maximum at 5.9 keV) improved from 1.36 keV at 60 °C to 0.73 keV at -20 °C. Neither the leakage current nor the capacitance of the GaAs detector were found to be the limiting factors of the energy resolution of the spectroscopic system; noise analysis at 0 °C and -20 °C revealed that the dominant source of noise was the quadratic sum of the dielectric and incomplete charge collection noise.

Keywords: Gallium Arsenide; GaAs; X-ray spectroscopy; wide bandgap; high temperature.

1. Introduction

The relatively low number of thermally generated carriers [1], high radiation hardness [2-5], and high stopping power [6] of GaAs devices, compared to traditional narrow bandgap semiconductor materials, such as Si, make them attractive options for a number of applications in radiation detection for space science [7] and medicine [8]. However, if GaAs devices are ever to replace traditional semiconductor X-ray detectors, such as Si photodiodes, further research is required to improve the maturity of GaAs technology. One of the areas needing development is material growth and processing [6].

The thickest and the best performing (in terms of energy resolution) GaAs X-ray detectors so far produced were grown by chemical vapor phase deposition (CVPD): ultrapure epitaxial layers of 40 μm [9], 150 μm [10], 325 μm [11], and 400 μm [12] thickness were successfully grown on n$^+$ semi-insulating GaAs substrates. The devices had a p$^+$-i-n$^+$ structure, with Au/Pt/Ti Schottky contacts on the p$^+$ layer, and guard rings. The devices had low leakage current densities at room temperature (as low as 4 nA/cm^2 [12]), and when coupled to ultra-low-noise preamplifier electronics, were able to achieve an energy resolution of 266 eV at 5.9 keV Full Width Half Maximum [9].

Energy resolutions as good as those reported by Owens et al. [9] have never since been replicated with GaAs X-ray spectrometers, despite considerable effort. The presence of impurities within the active volume of GaAs detectors can lead to charge carrier trapping and recombination, which has two direct effects in the detector's spectroscopic performance: 1) reduction in the signal amplitude, and 2) energy resolution degradation due to additional statistical fluctuations in the signal charge [13]. The probability of charge carrier trapping/recombination increases with increased device thickness, and thus, when this is a dominant effect, it places limitations on the thickness of GaAs devices that can still achieve an adequate energy resolution. However, this is balanced with the need for thick active layer GaAs X-ray detectors due to the reduction of the white series noise contribution of the X-ray detector and the increase of its quantum detection efficiency, as the active layer thickness increases.

---

a) Corresponding author. Tel.: +44 (0) 1273 872568.

54

55 Research has also been conducted on GaAs p^+-i-n^+ mesa X-ray photodiodes with progressively increasing
56 thicknesses; devices with i layer thicknesses of 2 μm [14] and 3 μm [15] (grown by MBE), and 7 μm [16] and
57 10 μm [17] (grown by metalorganic vapor phase epitaxy, MOVPE) have been produced and characterized for
58 their spectroscopic X-ray detection performance.

59

60 A lot of effort has been made on trying to identify the advantages and drawbacks of each growth technique,
61 LPE, MBE, and MOVPE, and relate the semiconductor device performance to its corresponding growth
62 method. LPE is the simplest, often the cheapest choice, and probably the appropriate method for industrial
63 production of thick X-ray photodiodes, however, it has given way in many applications to more versatile
64 techniques with higher flexibility and growth controllability (MBE and MOVPE) [18]. Although CVPD
65 produces extremely high-purity material, MBE has the potential to be the most precise epilayer growth
66 technique, potentially giving unparalleled control and reproducibility. Furthermore, it does not involve toxic
67 gas sources (e.g. arsine) unlike CVPD [6] [18]. However, it should be noted that MBE is a slow growth
68 technique and it may result in the introduction of defects [6]. The potentially higher defect level of structures
69 grown by MBE compared to that grown by MOVPE is not inherent to the technique [19]; previous studies
70 comparing the defect level of III-V structures grown by MBE and MOVPE [20 – 22], were not conclusive.
71 The discernment of which growth technique is better, is neither simple nor straightforward.

72

73 Here, results are reported characterizing a GaAs X-ray detector (p^+-i-n^+ photodiode with a 30 μm thick i layer)
74 as a function of temperature. The structure was grown by molecular beam epitaxy (MBE).

75

76 **2. Device structure**

77

78 The GaAs p^+-i-n^+ mesa photodiode was grown and fabricated at University of Nottingham, UK. The epitaxial
79 material was grown by MBE on a commercial n^+ GaAs substrate. A summary of the detector structure is
80 presented in **Table 1**. The unintentionally doped i layer had a thickness of 30 μm. The 0.5 μm thick p^+ layer
81 was doped with C at a doping density of 2×10^{18} cm^{-3}. On top of this, a 10 nm thick p^+ contact layer was
82 grown, doped with C at a doping density of 1×10^{19} cm^{-3}. The 1 μm thick n^+ layer was doped with Si at a
83 doping density of 2×10^{18} cm^{-3}. The circular mesa diode of a 400 μm diameter (area of 0.126 mm^2) was etched
84 using orthophosphoric acid : hydrogen peroxide : water, (1:1:1). The top Ohmic contact, covering 33% of the
85 area of the device, consisted of Au/Zn/Au (15/30/150 nm). The rear Ohmic contact consisted of Ge/Au/Ni/Au
86 (10/45/15/150 nm). The GaAs device was unpassivated.

87

88 **[Table 1]**

89

90 During the GaAs epitaxial growth, imperfections started to form. From the nucleation stage, and through the
91 epitaxial growth, butterfly defects formed. An optical microscope photograph showing the defects in one
92 detector can be seen in **Fig. 1 (a)**. The characteristic butterfly shape of the defects can be clearly seen at higher
93 magnification in **Fig. 1 (b)**.

94

95 **[Figure 1].**

96

97 The X-ray quantum detection efficiency of the structure, defined as the ratio between photons absorbed in the
98 active region and photons incident on the face of the structure, could not be measured directly with sufficient
99 certainty to add value to the manuscript. It was calculated using the Beer-Lambert law, taking into account
100 attenuation of X-rays within the top dead layers (i.e. the Ohmic contact and the GaAs 10 nm thick p^+ contact
101 layer) and absorption of X-rays within the active layers. In addition to the unintentionally doped i layer, the
102 p^+ layer was assumed to be active, since the electron diffusion length in GaAs with 2×10^{18} cm^{-2} doping density
103 is > 0.5 μm [23]. Similarly, the whole of the n^+ layer was considered to be active, since the hole diffusion
104 length in GaAs with 2×10^{18} cm^{-2} doping density is ≈ 1 μm [24]. For comparison, the X-ray absorption
105 characteristics of three different i layer thicknesses of GaAs were also calculated, and can be seen in **Fig. 2** for
106 photon energies up to 20 keV. Although the GaAs device reported here had an i layer thickness of 30 μm, the
107 maximum depletion layer width was 14 μm, see **Section 3.2. Capacitance measurements**. The linear
108 attenuation coefficients for Au and Zn (top Ohmic contact) and GaAs (p^+ contact layer) were extracted from

109   Henke et al. [25], whereas the linear absorption coefficients for GaAs (p$^+$, i, and n$^+$ layers) were extracted from
110   Cromer and Liberman [26]. The X-ray absorption fraction at 5.9 keV (and 6.49 keV) was calculated to be
111   0.59 (and 0.50) for a 10 µm GaAs layer, 0.69 (and 0.61) for a 14 µm GaAs layer, and 0.89 (and 0.84) for a 30
112   µm GaAs layer. These results emphasize the importance of a thick GaAs absorption layer for an X-ray
113   spectrometer when it is desirable to detect a large proportion of the incident X-ray flux, for example to reduce
114   spectra accumulation times. It should be noted here that the potentially increased incomplete charge collection
115   with increased i layer thickness is not reflected in the calculations of quantum efficiency shown in **Fig. 2**.

117   **[Figure 2]**

119   **3. Electrical characterization**

121   **3.1. Dark current measurements**

123   The current of the packaged GaAs photodiode detector was measured as a function of temperature under dark
124   conditions using a Keithley 6487 Picoammeter/Voltage Source. The temperature, initially set to 60 °C and
125   decreased to -20 °C, in 20 °C steps, was controlled by a TAS Micro LT climatic cabinet. The photodiode was
126   mounted in a light tight Al enclosure, inside the climatic cabinet. A dry environment (5% relative humidity)
127   was produced by dry N_2 continually flowing into the climatic cabinet throughout the measurements. Since the
128   GaAs photodiode was packaged in a TO-5 package, the leakage current associated with the device's package
129   was also measured across the same bias and temperature range as the packaged GaAs detector. The dark
130   current of the GaAs photodiode, with the parasitic leakage current of the package subtracted, can be seen in
131   **Fig. 3** across the temperature range 60 °C to -20 °C.

133   **[Figure 3]**

135   Both the forward and the reverse biased dark currents of the GaAs detector were found to be temperature
136   dependent. The saturation current and the ideality factor of the detector were extracted from the forward biased
137   current measurements (**Fig. 3 (a)**) [17]. The calculated saturation current, shown in **Fig. 4**, was found to
138   decrease from 32.8 pA ± 0.1 pA (26.1 nA/cm^2 ± 0.1 nA/cm^2) at 60 °C, to 4.07 fA ± 0.05 fA (3.24 pA/cm^2 ±
139   0.04 pA/cm^2) at -20 °C. These values were comparable with previously reported GaAs mesa photodiodes; for
140   example, saturation current densities of 17 nA/cm^2 ± 2 nA/cm^2 and 3.0 pA/cm^2 ± 0.3 pA/cm^2 were calculated
141   at 60 °C and -20 C, for GaAs photodiodes with 10 µm i layers [17]. The ideality factor, 1.944 ± 0.008 (rms
142   deviance), was found to be constant within the investigated temperature range. Since the ideality factor was
143   close to two, it suggested that the recombination current defined the forward current throughout the
144   temperature range investigated [27].

146   **[Figure 4]**

148   The leakage current of the detector at the maximum investigated applied reverse bias, -100 V (corresponding
149   to an applied electric field of 33 kV/cm), was found to decrease from 1.247 nA ± 0.005 nA (= 0.992 µA/cm^2
150   ± 0.004 µA/cm^2) at 60 °C to 16.0 pA ± 0.5 pA (= 12.8 nA/cm^2 ± 0.4 nA/cm^2) at -20 °C. Assuming the leakage
151   current originated from the bulk, the leakage current density at -100 V reverse bias was calculated by dividing
152   the leakage current at -100 V reverse bias by the area of the device. **Figure 5** shows the leakage current density
153   at -100 V reverse bias (33 kV/cm) as a function of temperature; the line of best fit was calculated using linear
154   least squares fitting. The leakage current density exponentially decreased as the temperature was reduced from
155   60 °C to -20 °C.

157   A previously reported GaAs photodiode, with a 40 µm thick epilayer grown by CVPD, had a leakage current
158   density of 92 nA/cm^2 at 25 kV/cm and 30 °C [28]. The currently reported detector had a leakage current
159   density of 91 nA/cm^2 at -75 V reverse bias (25 kV/cm) at 30 °C (interpolated). However, at 60 °C, this detector
160   had higher leakage current density than a different, previously reported, thinner (10 µm i layer) GaAs
161   photodiode fabricated from a structure grown by MOVPE [17]. At this temperature, a leakage current of 1
162   µA/cm^2 was measured using the present detector, whereas the thinner detector's leakage current density was
163   just 0.08 µA/cm^2 [17]; both devices were measured at an applied field strength of 33 kV/cm. The different

164 leakage current density between the GaAs device grown by MOVPE and the presently reported thicker GaAs
165 device grown by MBE, may be attributed to the increased defect density of the currently reported GaAs device
166 arising from the different epitaxial growth technique and/or the different thickness of the i layer. The presence
167 of a leakage current component arising from the mesa edges (surface leakage) cannot be excluded. Crystalline
168 defects, such as the butterfly defects present in the reported device, may lead to increased conductivity and
169 leakage current [6]. The surface and bulk components of the leakage current could be separated by measuring
170 the total leakage current of devices with different area. If the contribution of the surface leakage current to the
171 total current is significant, optimisation of the device fabrication procedure, including etchant recipe, and
172 possibly the addition of sidewall surface passivation, may reduce the surface leakage current [29].

174 **[Figure 5]**

176 **3.2. Capacitance measurements**

178 The depletion width and effective carrier concentration of the i layer of the detector was extracted from
179 capacitance measurements made as functions of both applied bias and temperature. The capacitance of the
180 packaged detector, C_{Dmeas}, was measured using an HP Multi Frequency LCR meter (50 mV rms magnitude and
181 1 MHz frequency test signal). The detector was placed inside a light tight Al enclose, which was then installed
182 inside a TAS Micro LT climatic cabinet for temperature control. To ensure thermal equilibrium, the
183 measurements at each temperature were started 30 minutes after the desired temperature was reached by the
184 climatic cabinet. A dry environment, <5% relative humidity, was maintained throughout the measurements
185 by continually flowing dry N_2 into the climatic cabinet.

187 The packaging capacitance, C_{pack}, defined as the capacitance between an empty pin (not wire bonded to a
188 diode) adjacent to the detector and the common pin of the package, was measured and subtracted from the
189 total measured capacitance of the packaged detector, in order to estimate the detector's own capacitance, C_D.
190 The total uncertainty associated with the detector capacitance was estimated to be ± 0.1 pF, whereas the
191 uncertainty associated with relative capacitance changes with temperature was estimated to be ± 0.02 pF. The
192 detector capacitance as a function of applied bias and temperature can be seen in **Fig. 6**.

194 **[Figure 6]**

196 The temperature dependence of the forward biased capacitance (**Fig. 6 (a)**) was attributed to the temperature
197 dependence of the forward current (**Fig. 3 (a)**), since the diffusion capacitance (which significantly contributes
198 to the forward biased capacitance) is directly proportional to the forward current [27]. The depletion layer
199 capacitance, which defines the reverse biased capacitance, decreased from 10.71 pF ± 0.02 pF at 60 °C to
200 10.10 pF ± 0.02 pF at -20 °C at zero applied bias, and from 1.007 pF ± 0.005 pF at 60 °C to 0.990 pF ± 0.005 pF
201 at -20 °C, at -100 V reverse bias. The most significant temperature variation of the reverse biased capacitance
202 occurred at low applied reverse biases, whereas an almost temperature invariant capacitance was measured at
203 high applied reverse biases.

205 The depletion layer width and effective carrier concentration of the i layer were computed using the measured
206 depletion layer capacitance [16]. The depletion layer width as a function of applied reverse bias at 20 °C can
207 be seen in **Fig. 7**. It increased from 1.4 μm ± 0.2 μm at 0 V applied bias, to 14 μm ± 1 μm at -100 V reverse
208 bias. At 60 °C, the depletion layer width at -100 V was 14.3 μm ± 0.1 μm; at -20 °C is was 14.5 μm ± 0.1 μm.
209 The uncertainties were determined by summating in quadrature the measurement uncertainties associated with
210 the capacitance measurements and the Debye length [27]. The Debye length was calculated to range from
211 0.1 μm at -20 °C to 0.2 μm at 60 °C for GaAs with a doping density of ~7.1×10^{14} cm^{-3}.

213 **[Figure 7]**

215 The effective carrier concentration of the GaAs detector at 20 °C was extracted from capacitance
216 measurements using the differential capacitance method [27]. The results are presented in **Fig. 8**. The effective
217 carrier concentration (**Fig. 8**) follows the i layer's doping profile when the doping profile does not have a sharp
218 gradient (spatial variation less than a Debye length) [30]. However, this general statement is true only in the

4

219 absence of electron traps. From **Fig. 8** it can be said that the effective carrier concentration was almost uniform
220 between 1.7 µm and 14 µm below the p$^+$-i junction, with a spatial resolution of a Debye length; a mean value
221 of 7.1×10^{14} cm^{-3} $\pm 0.7 \times 10^{14}$ cm^{-3} (rms deviance) was calculated. The derived effective carrier profile in the
222 i layer limited the depletion width to 14 µm $\pm$ 1 µm, when the maximum reverse bias was applied (-100 V).
223 This is similar to Bertuccio et al. [28], where a GaAs p$^+$-i-n$^+$ device with 40 µm thick i layer (grown by CVPD)
224 and a free carrier concentration of 1.5×10^{14} cm^{-3} had its active region depletion depth limited to 32 µm
225 at -100 V applied reverse bias. Although higher, the effective carrier concentration in the i layer grown by
226 MBE (7.1×10^{14} cm^{-3}) was of the same order of magnitude compared to the structure grown by CVPD ($1.5 \times$
227 10^{14} cm^{-3}) [28]. However, the difference in the carrier concentration of the currently reported MBE grown
228 device (7.1×10^{14} cm^{-3}) and the CVPD grown device (1.5×10^{14} cm^{-3}) had a great effect on the achieved
229 depletion layer width at a given applied reverse bias; 14 µm and 32 µm depletion width was achieved at -100 V
230 reverse bias at the MBE and CVPD grown device, respectively.

232 **[Figure 8]**

234 ## 4. ^{55}Fe photon counting X-ray spectroscopy

236 ### 4.1. ^{55}Fe radioisotope X-ray source measurements

238 An ^{55}Fe radioisotope X-ray source (Mn Kα = 5.9 keV, Mn Kβ = 6.49 keV) with an activity of 162 MBq was
239 positioned 3 mm above the GaAs detector. The detector was connected to a custom-made, single-channel,
240 charge-sensitive preamplifier of a feedback-resistorless design similar to that reported by Bertuccio et al. [31].
241 The input transistor of the preamplifier was a Vishay Siliconix 2N4416A Si JFET [32]. The
242 detector/preamplifier assembly was installed inside a TAS Micro LT climatic cabinet throughout the
243 measurements for temperature control. The temperature was initially set to 60 °C and decreased to -20 °C, in
244 20 °C steps with the same experimental procedure as was used for the electrical characterization. An Ortec
245 572A shaping amplifier was used to shape the output signal of the preamplifier, and an Ortec EASYMCA 8k
246 multi-channel analyser (MCA) was used for digitization.

248 ^{55}Fe X-ray spectra were collected at each temperature as a function of applied reverse bias, from -10 V
249 to -100 V, with a -10 V voltage step. The shaping time, τ, was kept constant at the shortest available (0.5 µs),
250 at temperatures $\geq$ 20 °C, given the relatively high leakage current of the detector as shown in **Fig. 3 (b)** (see
251 **4.2 Noise analysis** Section). In order to assist the noise analysis of the system, and identify the different noise
252 contributions, ^{55}Fe X-ray spectra were obtained as a function of shaping time (0.5 µs, 1 µs, 2 µs, 3 µs, 6 µs,
253 and 10 µs) at 0 °C and -20 °C, at applied reverse biases of -20 V, -40 V, -60 V, -80 V, and -100 V. A live time
254 of 60 s used to achieve adequate counting statistics. **Fig. 9** shows the spectrum with the best energy resolution
255 (Full Width at Half Maximum, *FWHM*, at 5.9 keV) obtained at 20 °C.

257 **[Figure 9]**

259 The characteristic Mn Kα (5.9 keV) and Mn Kβ (6.49 keV) lines of the ^{55}Fe radioisotope X-ray source could
260 not be resolved individually; hence the detected photopeak was the combination of the Mn Kα and Kβ lines.
261 Gaussians were fitted to the peaks taking into account both the relative emission ratio [33] and the relative
262 efficiency of the detector at 5.9 keV and 6.49 keV (**Fig. 2**). Each spectrum was energy calibrated using the
263 centroid channel number of its fitted Mn Kα peak and the position of the spectrum's zero energy noise peak.
264 The *FWHM* at 5.9 keV was measured for all accumulated spectra. A *FWHM* at 5.9 keV of 0.86 keV was
265 measured at 20 °C, when the detector was at -40 V applied reverse bias, and the shaping time was 0.5 µs. The
266 low energy tailing of the ^{55}Fe X-ray photopeak, i.e. counts at the left hand side of the photopeak outside of the
267 fitted Gaussian, seen in **Fig. 9**, and indeed in all the other obtained spectra, was attributed to partial charge
268 collection of charge created in the non-active layers of the device. The valley-to-peak ratio (*V/P*) was
269 calculated for the accumulated spectra at 20 °C as a function of applied reverse bias, from the ratio between
270 the number of counts at the valley of the low energy tailing (channel number corresponding to 4 keV) and the
271 number of counts at the centroid channel of the fitted Gaussian at 5.9 keV. This can be seen in **Fig. 10** as a
272 function of applied reverse bias and depletion layer width.

274 **[Figure 10]**
275
276 The valley-to-peak ratio improved from 0.34 at -10 V applied reverse bias (depletion width of 4 μm) to 0.09
277 at -70 V applied reverse bias (depletion layer width of 12 μm), and remained stable up to -100 V applied
278 reverse bias (depletion layer width of 14 μm). The valley-to-peak ratio improvement with increased applied
279 bias may be attributed to the improvement of the energy resolution (*FWHM* at 5.9 keV); the energy resolution
280 was found to improve from 1.08 keV at -10 V applied reverse bias to 0.86 keV at -40 V applied reverse bias
281 (see **Fig. 12**).
282
283 The improvement of the valley-to-peak ratio with increased applied reverse bias was also attributed to the
284 increase of the depletion layer width (active layer) with increased applied reverse bias, which resulted in an
285 increase of the ratio between the thicknesses of the active and non-active layers.
286
287 Reduced charge trapping at high electric fields may also explain the observed improvement in valley-to-peak
288 ratio as the applied reverse bias was increased. Improved charge transport may have increased the number of
289 counts contributing to the 5.9 keV photopeak and removed counts from the valley at the same time. In order
290 to investigate the contribution of reduced charge trapping to the observed valley-to-peak ratio, the total number
291 of counts within the fitted Mn Kα Gaussian was measured for all spectra accumulated at 20 °C. The number
292 of counts within the Gaussian as a function of detector applied reverse bias and depletion width can be seen in
293 **Fig. 11**.
294
295 **[Figure 11]**
296
297 The number of counts in the Mn Kα Gaussian increased from 1.20×10^5 at -10 V applied reverse bias (depletion
298 layer width of 4 μm) to 2.21×10^5 at -100 V applied reverse bias (depletion layer width of 14 μm). The number
299 of counts in the Mn Kα peak was expected to increase with increased depletion layer as per the Beer-Lambert
300 law. The number of counts expected to be detected in the Kα peak at each depletion width, was calculated by
301 taking into account the relative quantum detection efficiency at each point compared to that at 14 μm (-100
302 V). The uncertainties associated with the prediction (shown in **Fig. 11**) reflect the uncertainties in the
303 calculated depletion width at each reverse bias (**Fig. 7**). The good agreement between the experimental and
304 predicted to be detected number of counts in the Mn Kα peak suggested that the improvement of the charge
305 transport with increased applied reverse bias was insignificant.
306
307 The *FWHM* at 5.9 keV as a function of applied reverse bias at each temperature and at 0.5 μs shaping time can
308 be seen in **Fig. 12**. The optimum reverse bias, which resulted in the best *FWHM* at 5.9 keV, was found to vary
309 with temperature. The best *FWHM* at 5.9 keV achieved at each investigated temperature can be seen in **Fig.
310 13**.
311
312 **[Figure 12]**
313
314 **[Figure 13]**
315
316 The *FWHM* at 5.9 keV decreased as the temperature decreased; it improved from 1.36 keV at 60 °C to 0.73
317 at -20 °C. Discussion and explanation of the results shown in **Fig. 12** and **Fig. 13** are presented in the following
318 section, along with the noise analysis of the X-ray spectroscopic system.
319
320 **4.2. Noise analysis**
321
322 The quadratic sum of three independent noise contributions, Fano noise, incomplete charge collection noise,
323 and electronic noise, defines the energy resolution of a non-avalanche photodiode X-ray spectrometer [34].
324 The Fano noise arises due to the statistical nature of the ionization process [35], whereas the incomplete charge
325 collection (*ICC*) noise arises due to carrier trapping and recombination as the results of crystal imperfections
326 [6]. The electronic noise consists of the white series noise (*WS*) (including the induced current noise), white
327 parallel noise (*WP*), 1/*f* noise (1/*f*), and the dielectric noise (*DN*) [34]. All noise components are functions of

328 temperature but different noise components have different dependencies upon the applied reverse bias and the
329 shaping time.
330
331 The white series noise is inversely proportional to the shaping time and depends on the total capacitance at the
332 input of the preamplifier. The total capacitance includes the packaged detector's capacitance (**Fig. 6** plus
333 package capacitance) the feedback capacitance, the input JFET capacitance, and any stray capacitances. The
334 white parallel noise is directly proportional to the shaping time and depends on the leakage current of the
335 detector (**Fig. 3**) and the input JFET. The Fano noise and the $1/f$ noise are both shaping time invariant and can
336 be readily calculated [34]. The dielectric noise and the incomplete charge collection noise are both shaping
337 time invariant, but the incomplete charge collection noise can vary greatly with applied reverse bias, whereas
338 the dependence of the dielectric noise on shaping time is nil.
339
340 The *FWHM* at 5.9 keV varied with applied reverse bias. This can be seen in **Fig. 12** where the *FWHM* is
341 presented at all temperatures at a shaping time of 0.5 μs. The energy resolution improved as the applied reverse
342 bias was increased (in magnitude) up to: -30 V at 60 °C; -40 V at 40 °C, 20 °C, and 0 °C; and -60 V at -20 °C.
343 Reduction of the incomplete charge collection noise (due to improved charge transport at increased internal
344 electric fields) and reduction of the white series noise (due to reduction of the detector's capacitance) with
345 increased applied bias may explain the observed energy resolution improvement. A further increase (in
346 magnitude) in the applied reverse bias from the limits stated above to -100 V, resulted in the deterioration of
347 the energy resolution. Increase of the white parallel noise (due to increased leakage current) with increased
348 applied bias may explain the observed energy resolution worsening (**Fig. 12**).
349
350 A multidimensional nonlinear minimization was applied to the measured *FWHM* equivalent noise charge
351 (*ENC*) at 5.9 keV (in e⁻ rms) as a function of shaping time as measured at 0 °C (-40 V applied reverse bias)
352 and -20 °C (-60 V applied reverse bias). The measured and fitted *ENC* at 5.9 keV at the two lowest investigated
353 temperatures can be seen in **Fig. 14**. The noise contributions proportional to shaping time (*WP* noise),
354 inversely proportional to shaping time (*WS* noise), and shaping time invariant, were identified. The Fano noise
355 and the $1/f$ noise were calculated as per Lioliou & Barnett [34], and were then subtracted in quadrature from
356 the shaping time invariant noise contribution in order to give the quadratic sum of the dielectric and incomplete
357 charge collection noise. All the different noise contributions as functions of shaping time, at 0 °C (-40 V
358 applied reverse bias) and -20 °C (-60 V applied reverse bias), can be seen in **Fig. 14**.
359
360 **[Figure 14]**
361
362 The white series noise contribution revealed the presence of 4.3 pF and 6.2 pF total capacitance at the input of
363 the preamplifier at 0 °C (-40 V applied reverse bias) and -20 °C (-60 V applied reverse bias), respectively. The
364 white parallel noise contribution revealed the presence of 9.2 pA and 5.8 pA total leakage current at 0 °C (-40
365 V applied reverse bias) and -20 °C (-60 V applied reverse bias), respectively. The Fano noise contribution at
366 5.9 keV, as calculated assuming a Fano factor of 0.12 [36] and a linear temperature dependence of the electron
367 hole pair creation energy (ε [eV] = 4.55 – 0.00122 T [K], [37]), was found to decrease from 129 eV at 0 °C to
368 128 eV at -20 °C. The $1/f$ noise, which is proportional to the total input capacitance, was found to increase
369 from 42 eV at 0 °C to 48 eV at -20 °C, due to the increase of the apparent total capacitance at the input of the
370 preamplifier.
371
372 The dominant source of noise, at 0 °C (-40 V applied reverse bias) and -20 °C (-60 V applied reverse bias) was
373 found to be the quadratic sum of the dielectric and incomplete charge collection noise. This was found to
374 decrease from 678 eV (equivalent noise charge of 68 e⁻ rms) at 0 °C and -40 V applied reverse bias to 637 eV
375 (equivalent noise charge of 64 e⁻ rms) at -20 °C and -60 V applied reverse bias. The dielectric noise was
376 expected to decrease with decreasing temperature, given its dependency on temperature [34]; this is consistent
377 with observations.
378
379 The best energy resolution (*FWHM* at 5.9 keV) at 20 °C achieved with the reported spectrometer was 860 eV.
380 For comparison purposes, previously reported spectrometers with similar preamplifier electronics employing
381 thinner GaAs p⁺-i-n⁺ photodiodes, fabricated from material grown by MOVPE, had better energy resolution
382 (*FWHM* at 5.9 keV) at 20 °C; 750 eV for a 7 μm i layer thick (200 μm diameter) [16], 730 eV for a 10 μm i

layer thick (400 μm diameter), and 690 eV for a 10 μm i layer thick (200 μm diameter) [17]. The broader *FWHM* at 5.9 keV of the currently reported spectrometer was the result of numerous factors. Even though the reported detector had a thicker i layer, its effective carrier profile in the i layer ($\sim 7.1 \times 10^{14}$ cm^{-3}, **Fig. 7**) limited its depletion width, thus providing a greater capacitance than would have been the case if the detector had been fully depleted. Additionally, the relatively high leakage current, which may have arisen from the material defects (as a consequence of the epitaxial growth technique and/or the thicker i layer) and/or the mesa edges and the possible presence of incomplete charge collection noise, resulted in broader *FWHM* at 5.9 keV. None of the above results (*FWHM* at 5.9 keV) were as good as the best results ever reported for GaAs p$^+$-i-n$^+$ detectors (thick i layers grown by CVPD) with Schottky contacts and guard rings (0.266 keV *FWHM* at 5.9 keV [9] and 0.300 keV *FWHM* at 5.9 keV [11] at room temperature). Part of the reason for achieving such good energy resolution in the results of Owens et al. and Erd et al. was minimization of dielectric noise by mounting the detector and input JFET of the preamplifier together in close proximity on the same low-loss substrate [9] [11], but the extremely high quality of the material was also a significant factor.

Despite having relatively high leakage current, limited depletion layer width, and possible incomplete charge collection noise, the reported GaAs detector was demonstrated to be spectroscopic for ^{55}Fe X-ray photons across a wide temperature range (60 °C to -20 °C) with moderate energy resolution.

5. Conclusions and future work

A 30 μm thick i layer GaAs p$^+$-i-n$^+$ photodiode detector (400 μm diameter circular mesa) fabricated from material grown by molecular beam epitaxy (MBE) was characterized for its electrical and photon counting X-ray spectroscopic performance across the temperature range 60 °C to -20 °C.

A temperature invariant ideality factor of 1.944 ± 0.008 suggested that the recombination current defined the forward current. The leakage current of the detector at the maximum investigated reverse bias, -100 V (33 kV/cm applied electric field) was found to decrease from 1.247 nA ± 0.005 nA (0.992 μA/cm^2 ± 0.004 μA/cm^2) at 60 °C to 16.0 pA ± 0.5 pA (12.8 nA/cm^2 ± 0.4 nA/cm^2) at -20 °C. The detector had a similar leakage current density as a previously reported high quality GaAs detector [28]. However, the leakage current density at high temperatures (60 °C) was greater than has been reported previously with thinner (10 μm i layer) GaAs detectors of similar geometry fabricated from material grown by MOVPE [17]. The presence of butterfly defects and/or surface leakage current may explain the relatively high leakage current measured.

When the detector was biased at -100 V, its capacitance was temperature invariant. A depletion layer width of 14 μm ± 1 μm in this bias condition across the temperature range was implied. A mean effective carrier concentration of 7.1×10^{14} cm^{-3} ± 0.7×10^{14} cm^{-3} (rms deviance) was calculated for the region of material between 1.7 μm and 14 μm below the p$^+$-i junction, which limited the depletion layer width.

The best energy resolution, *FWHM* at 5.9 keV, achieved when the detector was coupled to a custom-made charge-sensitive preamplifier improved from 1.36 keV at 60 °C to 0.73 keV at -20 °C. Noise analysis of data collected at 0 °C and -20 °C revealed that the shaping time invariant noise, i.e. the quadratic sum of the dielectric and incomplete charge collection noise, was the dominant contributor. This was found to decrease from 678 eV (equivalent noise charge of 68 e$^-$ rms) at 0 °C and -40 V applied reverse bias, to 637 eV (equivalent noise charge of 64 e$^-$ rms) at -20 °C and -60 V applied reverse bias.

The reported device was usable as the detector for a photon counting X-ray spectrometer which operated across an 80 °C wide temperature range (60 °C – -20 °C) without cooling. Work to improve the material quality of thick GaAs layers for X-ray spectrometers will be conducted and reported in future publications.

437

DATA AVAILABILITY
Data underlying this work are subject to commercial confidentiality. The Authors regret that they cannot grant public requests for further access to any data produced during the study, however the key findings are fully included within the article.

REFERENCES

[1] G. Bertuccio, C. Canali, G. De Geronimo, C. Lanzieri, A. Longoni, and F. Nava, F., IEEE Trans. Nucl. Sci. **46**, 1999, 1209.

[2] T. Ly Anh, A. Perd'ochová, V. Nečas, and V. Pavlicová, Nucl. Phys. B Proc. Suppl.**150**, 2006, 402.

[3] M. Ladzianský, A. Šagátová, V. Nečas, F. Dubecký, and V. Linhart, Nucl. Instrum. Meth. Phys. Res. A **607**, 2009, 135.

[4] A. Šagátová, B. Zat'ko, M. Pavlovič, K. Sedlačková, P. Hybler, F. Dubecký, and V. Nečas, J. Instrum. **9**, 2014, C04036.

[5] V.K. Dixit, S.K. Khamari, S. Manwani, S. Porwal, K. Alexander, T.K. Sharma, S. Kher, and S.M. Oak, Nucl. Instrum. Meth. Phys. Res. A **785**, 2015, 93.

[6] A. Owens, Compound Semiconductor Radiation Detectors, CRC Press, Florida; 2012.

[7] J. Huovelin, R. Vainio, H. Andersson, E. Valtonen, L. Alha, A. Mälkki, M. Grande, G.W. Fraser, M. Kato, H. Koskinen, K. Muinonen, J. Näränen, W. Schmidt, M. Syrjäsuo, M. Anttila, T. Vihavainen, E. Kiuru, M. Roos, J. Peltonen, J. Lehti, M. Talvioja, P. Portin, and M. Prydderch, Planet. Space Sci. **58**, 2010, 96.

[8] D. Kozhevnikov, G. Chelkov, M. Demichev, A. Gridin, P. Smolyanskiy, and A. Zhemchugov, J. Instrum. **12**, 2017, C01005.

[9] A. Owens, M. Bavdaz, A. Peacock, A. Poelaert, H. Andersson, S. Nenonen, H. Sipila, L. Tröger, and G. Bertuccio, G., J. Appl. Phys. **90**, 2001, 5376.

[10] A. Owens, H. Andersson, M. Campbell, D.H. Lumb, S.A.A. Nenonen, and L. Tlustos, Proc. SPIE, Astronomical Telescopes + Instrumentation, **5501**, 2004, 241.

[11] C. Erd, A. Owens, G. Brammertz, M. Bavdaz, A. Peacock, V. Lämsä, S. Nenonen, H. Andersson, and N. Haack, Nucl. Instrum. Meth. Phys. Res. A **487**, 2002, 78.

[12] A. Owens, A.J. Peacock, and M. Bavdaz, Proc. SPIE, X-ray and Gamma-Ray Telescopes and Instruments for Astronomy, **4851**, 2003,1059.

[13] G. Bertuccio, C. Canali, and F. Nava, Nucl. Instrum. Meth. Phys. Res. A **410**, 1998, 29.

[14] A.M. Barnett, J.E. Lees, D.J. Bassford, J.S. Ng, C.H. Tan, N. Babazadeh, and R.B. Gomes, Nucl. Instrum. Meth. Phys. Res. A **654**, 2011, 336.

[15] A.M. Barnett, Nucl. Instrum. Meth. Phys. Res. A **756**, 2014, 39.

[16] G. Lioliou, X. Meng, J.S. Ng, and A.M. Barnett, J. Appl. Phys. **119**, 2016, 124507.

[17] G. Lioliou, M.D.C. Whitaker, and A.M. Barnett, A.M., J. Appl. Phys. **122**, 2017, 244506.

[18] P. Capper, S. Irvine, and T. Joyce, Epitaxial Crystal Growth: Methods and Materials, in Handbook of Electronic and Photonic Materials, Springer International Publishing, Cham: 2017.

[19] R. Pelzel, Proc. CS MANTECH, New Orleans, 2013, 105.

[20] S.P. Tobin, S.M. Vernon, C. Bajgar, S. Wojtczuk, M.R. Melloch, A. Keshavarzi, T.B. Stellwag, S. Venkatensan, M. Lundstrom, and K.A. Emery, IEEE Trans. Nucl. Sci. 37, 1990, 469.

[21] A.J. Ptak, S.W. Johnston, S. Kurtz, D.J. Friedman, and W.K. Metzger, J. Cryst. Growth 251, 2003, 392.

[22] D.J. Chmielewski, K. Galiano, P. Paul, D. Cardwell, S. Carnevale, J.A. Carlin, A.R. Arehart, T.J. Grassman, and S.A. Ringel, Proc. IEEE PVSC, Portland, 2016, 3411.

[23] L.W. Aukerman, M.F. Millea, and M. McColl, J. Appl. Phys. **38**, 1967, 685.

[24] C.J. Hwang, J. Appl. Phys. **40**, 1969, 3731.

[25] B.L. Henke, E.M. Gullikson, and J.C. Davis, At. Data Nucl. Data Tables **54**, 1993, 181.

[26] D.T. Cromer, and D. Liberman, Relativistic Calculation of Anomalous Scattering Factors for X-rays, LASL Report LA-4403, New Mexico: 1970.

[27] S.M. Sze, and K.K. Ng, Physics of Semiconductor Devices, 3rd ed., John Wiley & Sons, New Jersey: 2007.

489   [28] G. Bertuccio, R. Casiraghi, D. Maiocchi, A. Owens, M. Bavdaz, A. Peacock, H. Andersson, and S.
490   Nenonen, IEEE Trans. Nucl. Sci. **50**, 2003, 723.
491   [29] M.S. Carpenter, M.R. Melloch, M.S. Lundstrom, and S.P. Tobin, Appl. Phys. Lett. **52**, 1988, 2157.
492   [30] R.A. Stradling, and P.C. Klipstein, Growth and Characterisation of Semiconductors, IOP Publishing Ltd,
493   Bristol: 1990.
494   [31] G. Bertuccio, P. Rehak, and D. Xi, Nucl. Instrum. Meth. Phys. Res. A **326**, 1993, 71.
495   [32] Siliconix, 2N4416/2N4416A/SST4416 N-Channel JFETs, Data Sheet, 70242 S-04028, Rev. F, 04 Jun 01,
496   Vishay Electronic GmbH, Selb: 2001.
497   [33] U. Schötzig, Appl. Radiat. Isot. **53**, 2000, 469.
498   [34] G. Lioliou, and A.M. Barnett, Nucl. Instrum. Meth. Phys. Res. A **801**, 2015, 63.
499   [35] U. Fano, Phys. Rev. **72**, 1947, 26-29.
500   [36] G. Bertuccio, A. Pullia, J. Lauter, A. Forster, and H. Luth, IEEE Trans. Nucl. Sci. **44**, 1997, 1.
501   [37] G. Bertuccio, and D. Maiocchi, J. Appl. Phys. **92**, 2002, 1248.

Table and figure captions

Table 1. Layers structure of the GaAs p$^+$-i-n$^+$ wafer.

Figure 1. (a) Optical microscope photograph of a GaAs device of the type produced and characterised in this work and (b) the butterfly defects shown as the imperfections across the material.

Figure 2. Quantum detection efficiency as a function of X-ray photon energy for the GaAs p$^+$-i-n$^+$ mesa photodiode with a structure shown in **Table 1**, with variable i layer thickness; 30 μm (solid line), 14 μm (dotted line), and 10 μm (dashed line) thick GaAs i layer.

Figure 3. Dark current of the GaAs detector as a function of (a) forward and (b) reverse applied bias at the temperature range 60 °C to -20 °C.

Figure 4. Saturation current as a function of temperature of the detector.

Figure 5. The GaAs detector's leakage current density at 33 kV/cm applied electric field as a function of temperature.

Figure 6. Capacitance of the GaAs detector as a function of (a) forward and (b) reverse applied bias within the temperature range 60 °C to -20 °C.

Figure 7. Depletion layer width as a function of applied reverse bias of the detector at 20 °C.

Figure 8. Effective carrier concentration at 20 °C as a function of distance below the p$^+$-i junction. The dotted line represents the mean effective carrier concentration as calculated between 1.7 μm and 14 μm below the p$^+$-i junction.

Figure 9. ^{55}Fe X-ray spectrum accumulated at 20 °C with the detector reversed bias at -40 V. Also shown are the fitted Mn Kα and Mn Kβ (dashed lines) peaks.

Figure 10. Valley-to-peak ratio (*V/P*) as a function of (a) applied reverse bias and (b) depletion layer width of the ^{55}Fe X-ray spectra accumulated with the GaAs diode, at 20 °C and 0.5 μs.

Figure 11. Number of counts in the fitted Mn Kα Gaussian as a function of (a) applied reverse bias and (b) depletion layer width, at a temperature of 20 °C and a shaping time of 0.5 μs. The relative number of counts expected to be detected at each applied reverse bias (and depletion width), according to the relative change of the detection efficiency compared to that at 14 μm (-100 V reverse bias), is also shown.

Figure 12. *FWHM* at 5.9 keV as a function of applied reverse bias and temperature, at a shaping time of 0.5 μs.

Figure 13. Best *FWHM* at 5.9 keV as a function of temperature at the optimum reverse bias and shaping time.

Figure 14. Equivalent noise charge, ENC, at 5.9 keV as a function of shaping time at (a) 0 °C (-40 V reverse bias) and (b) -20 °C (-60 V reverse bias). The noise contributions are also shown: white series, *WS*, (round dots); white parallel, *WP*, (dashes); Fano (solid line); 1/*f* (dashes dots); quadratic sum of dielectric, *DN*, and incomplete charge collection, *ICC*, noise (long dashes). The contributions were determined from a multidimensional least squares fitting (double solid line) of the experimental points (filled circles).

Figure 1

(a)

(b)

Figure 2

(a)

(b)

Figure 4

Figure 5

$J_R = 3.3 \times 10^{-8} e^{(0.05T\,[°C])}$

33 kV/cm

(a)

(b)
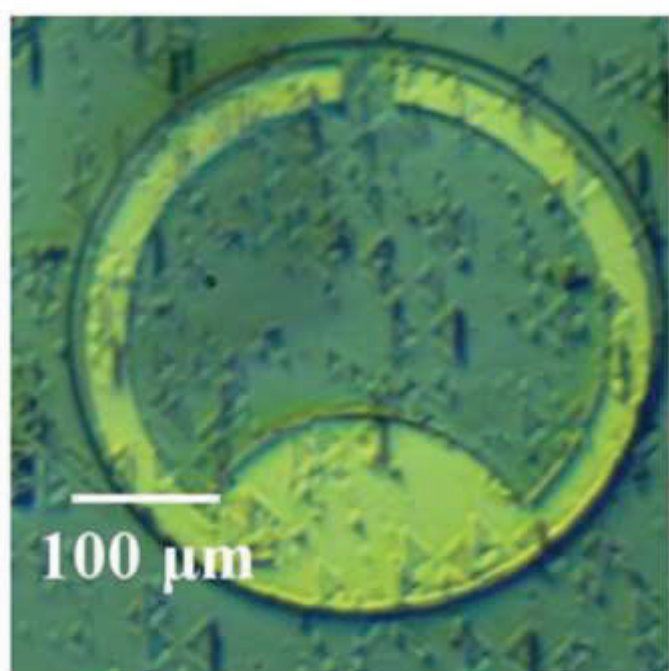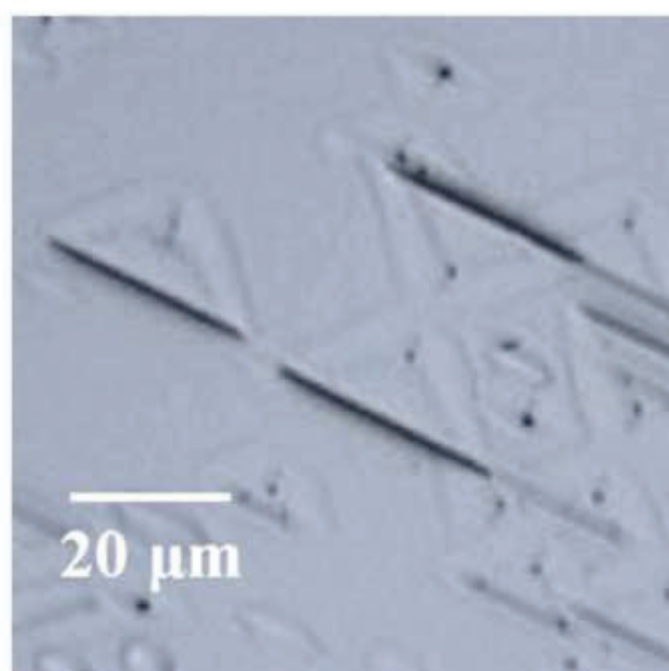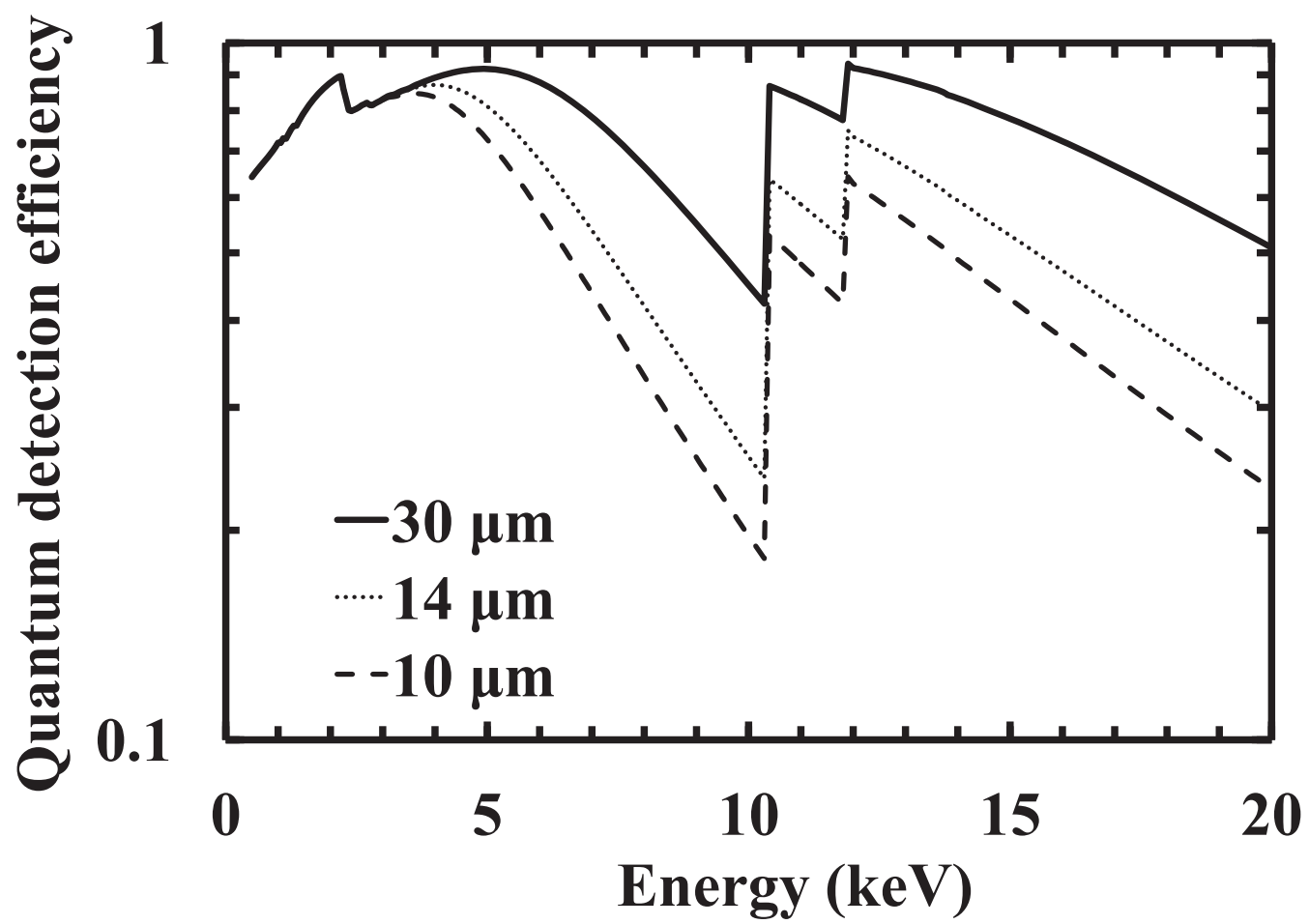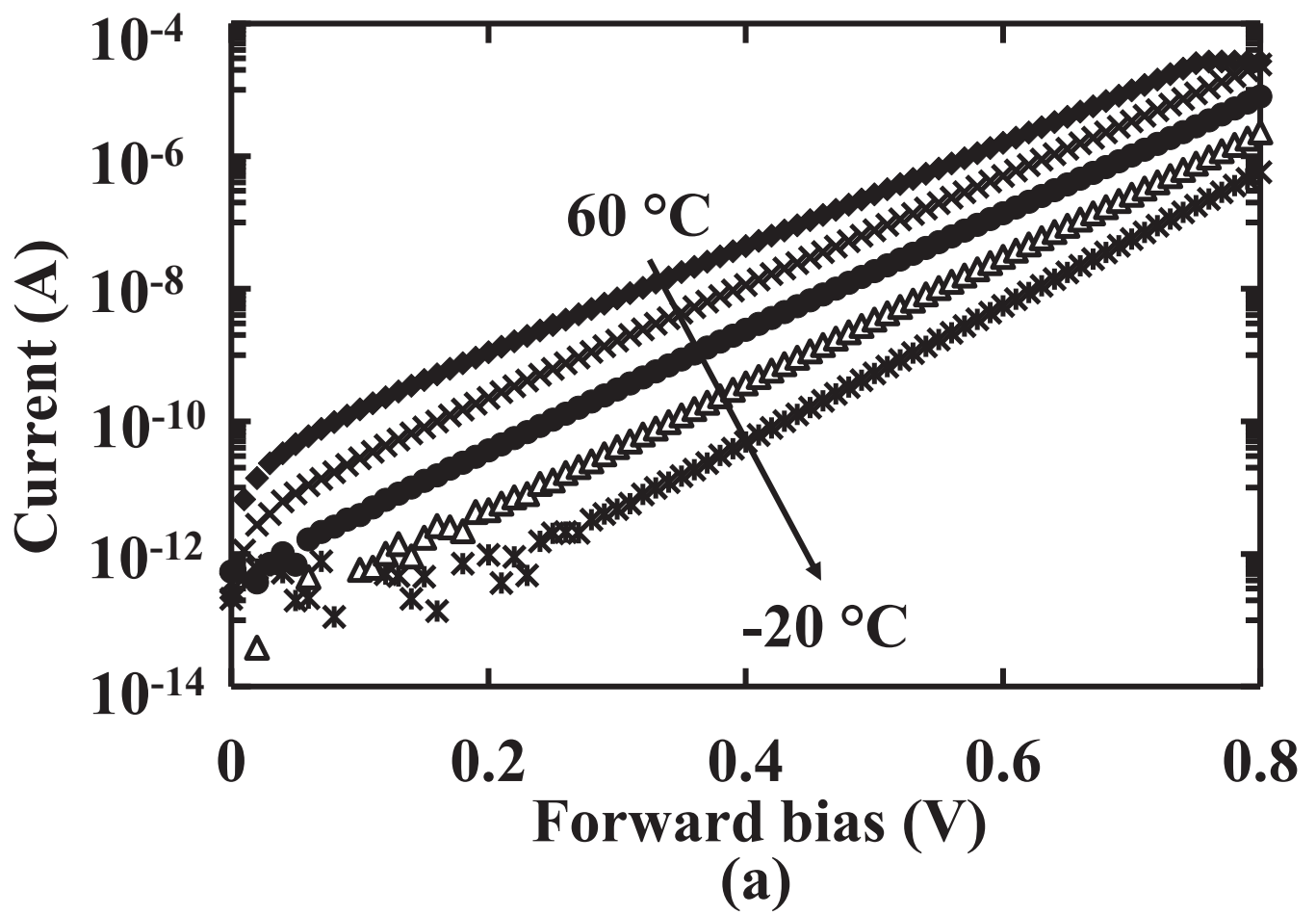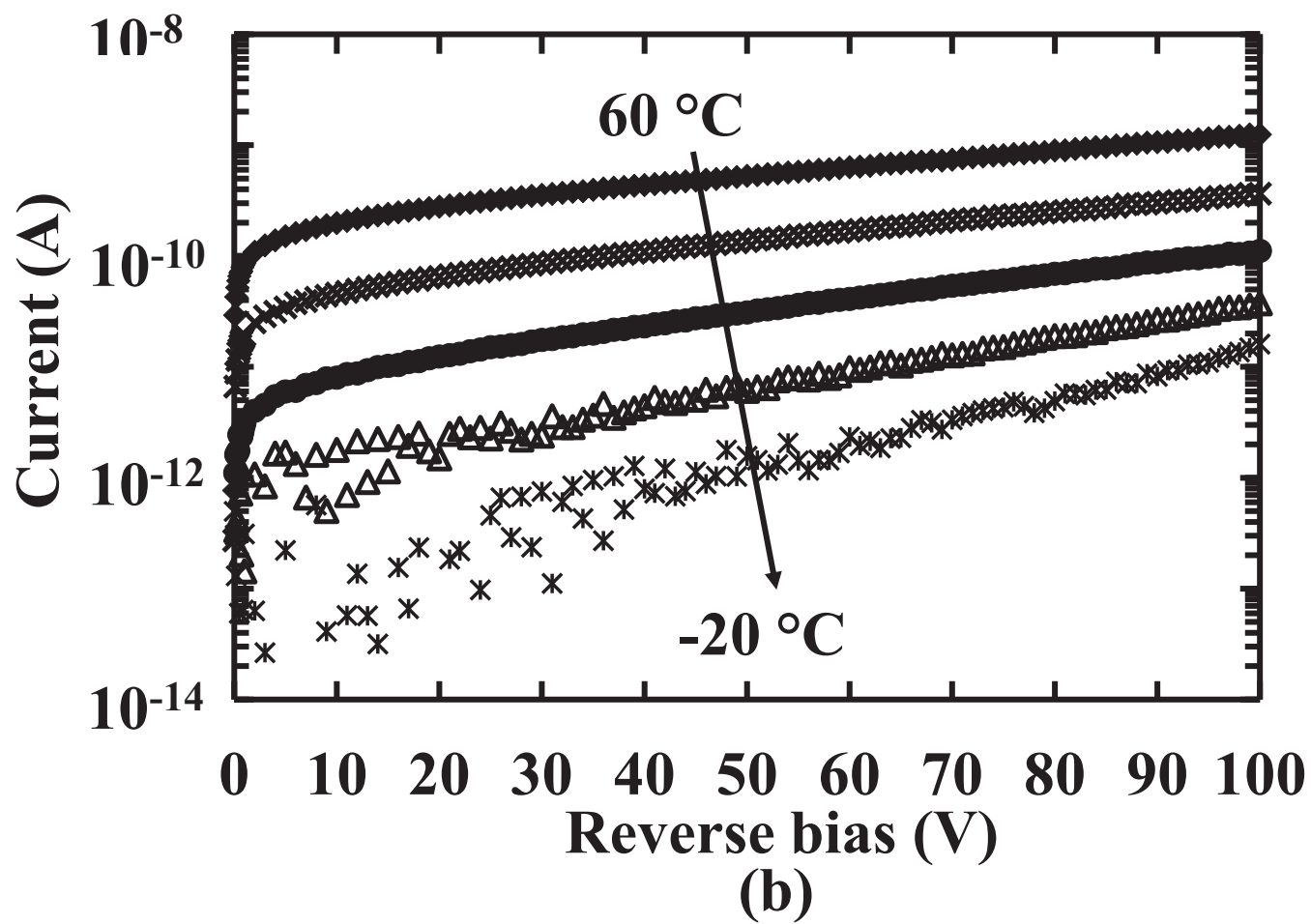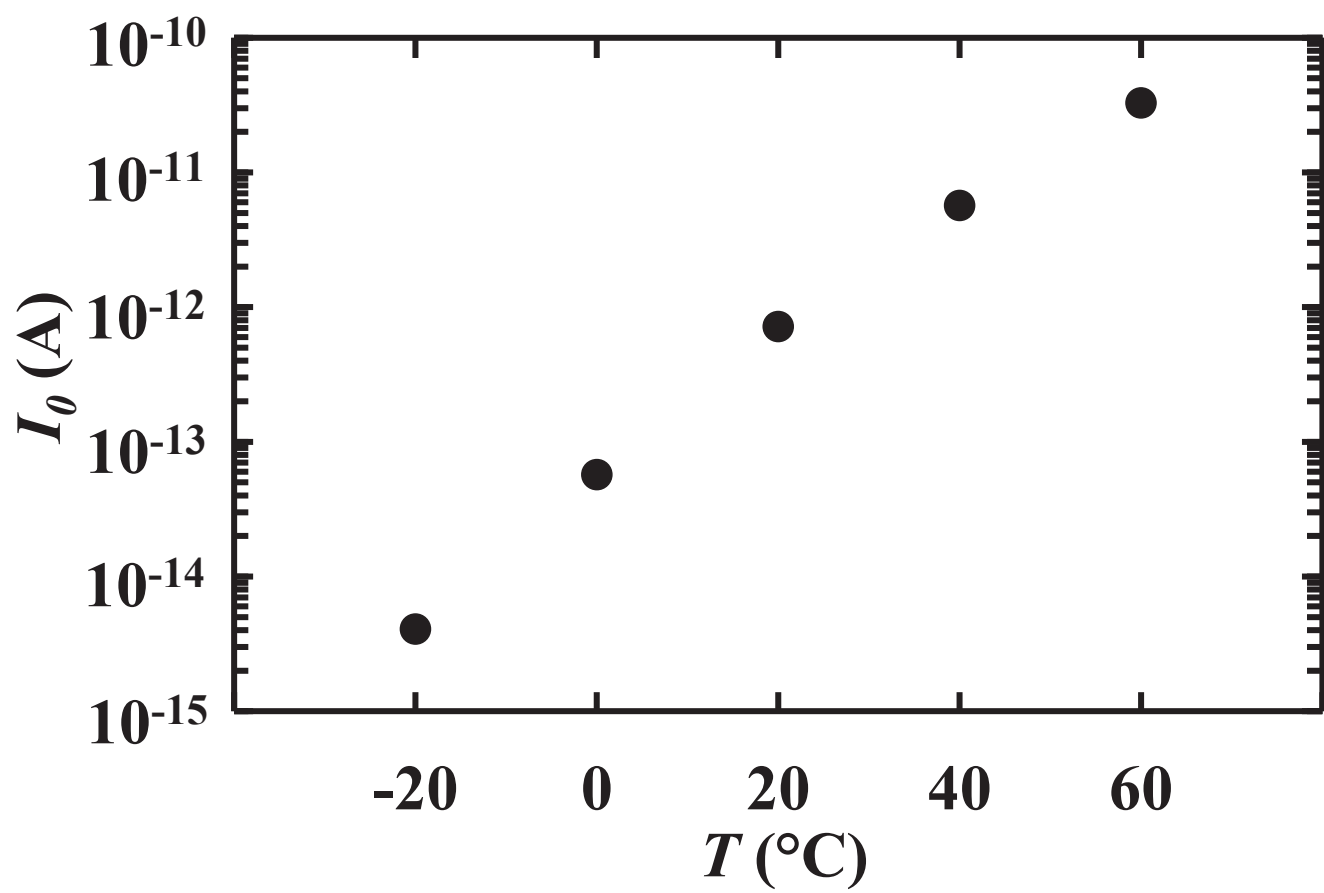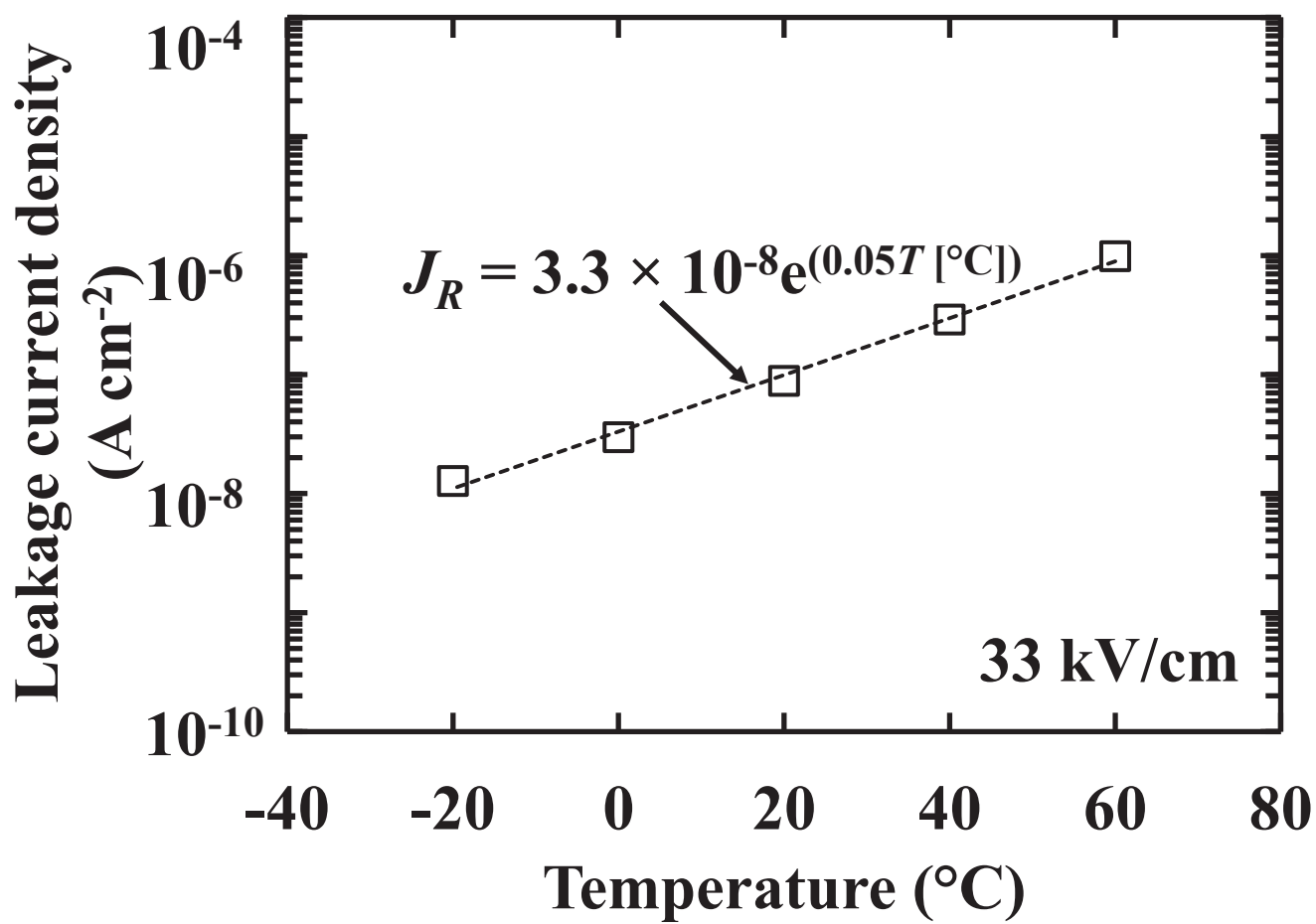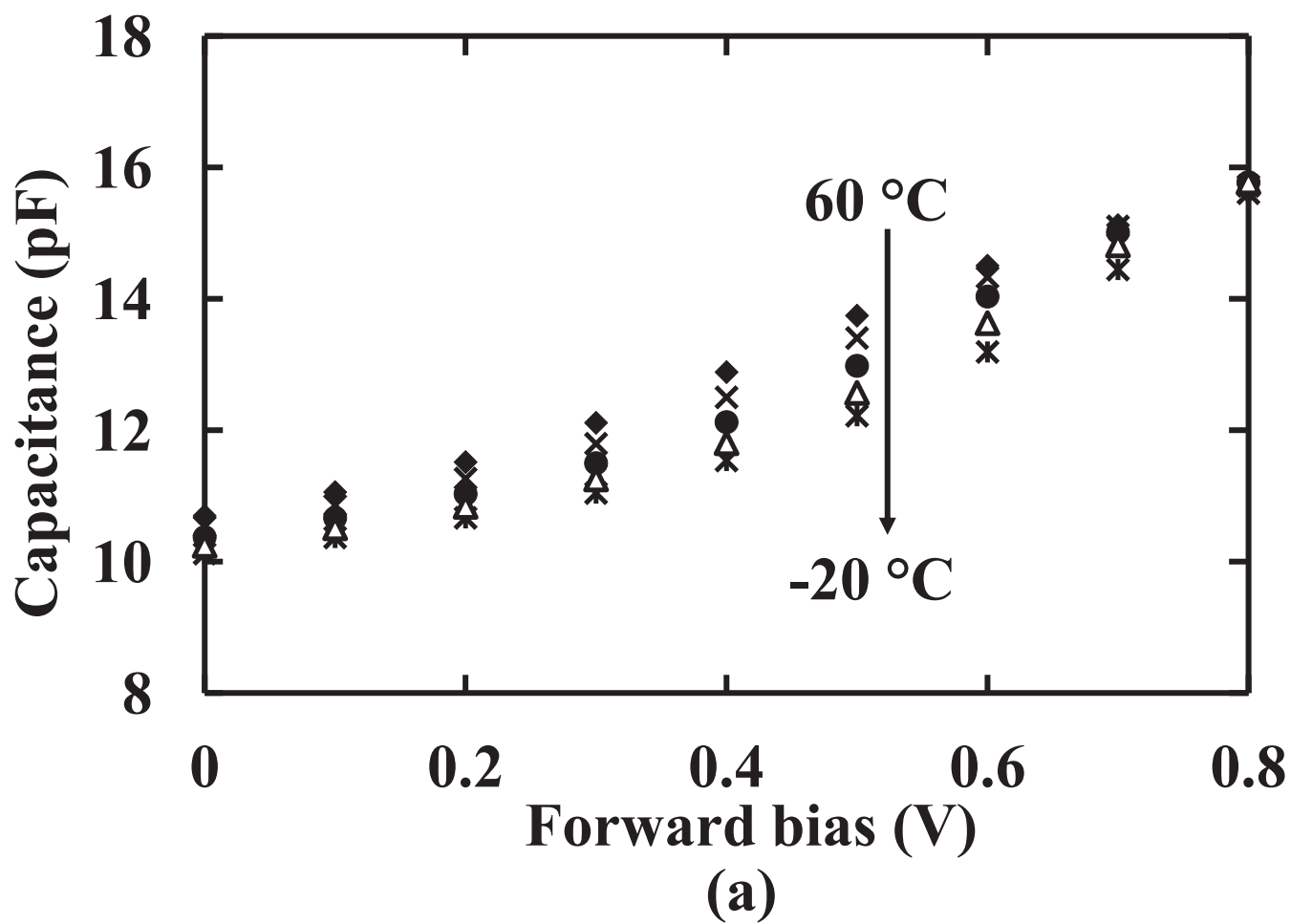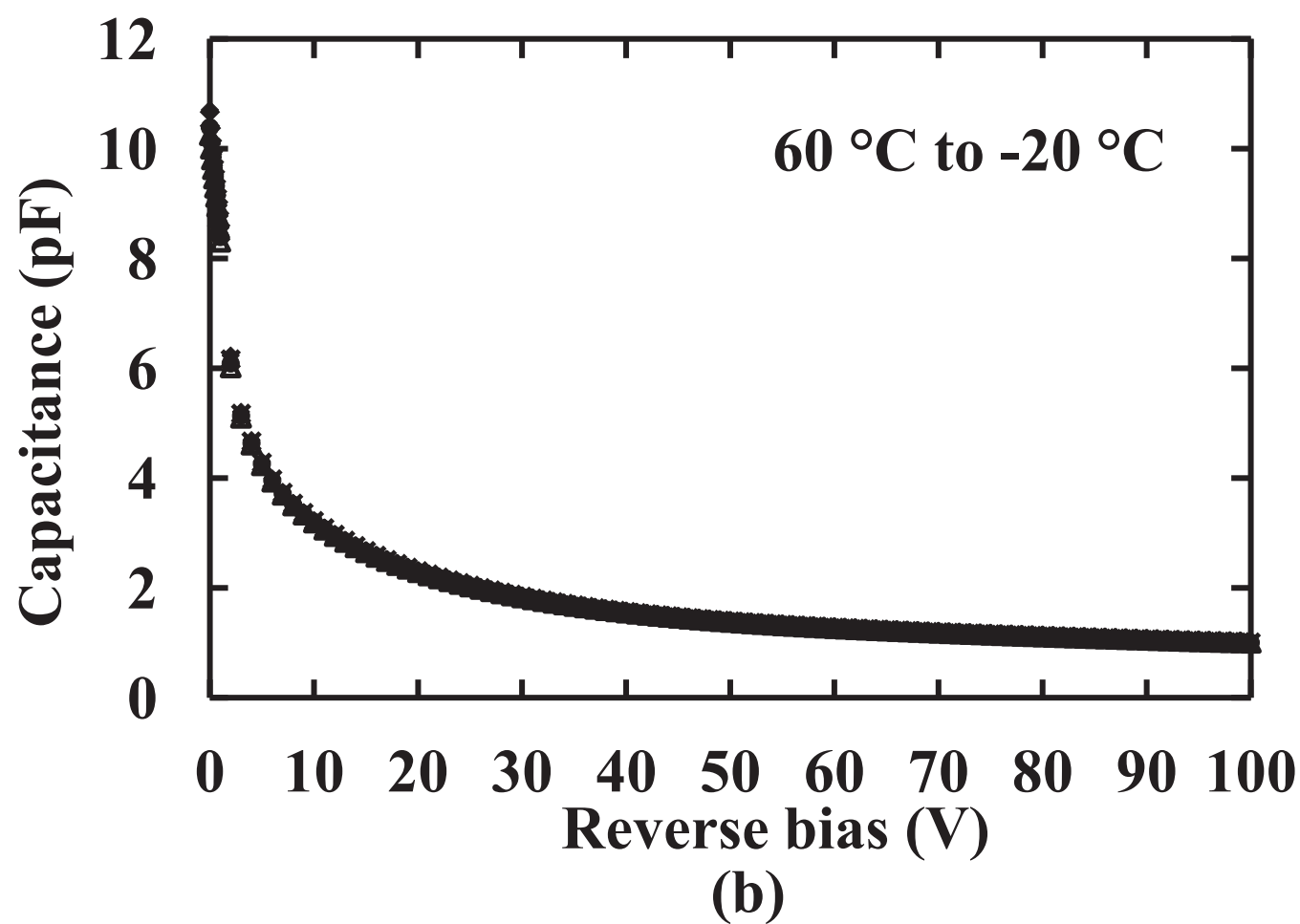
Figure 7

Figure 7

Figure 8

Figure 9

FWHM at 5.9 keV = 0.86 keV

T = 20 °C
V_{AR} = -40 V
τ = 0.5 μs

(a)

(b)

(a)
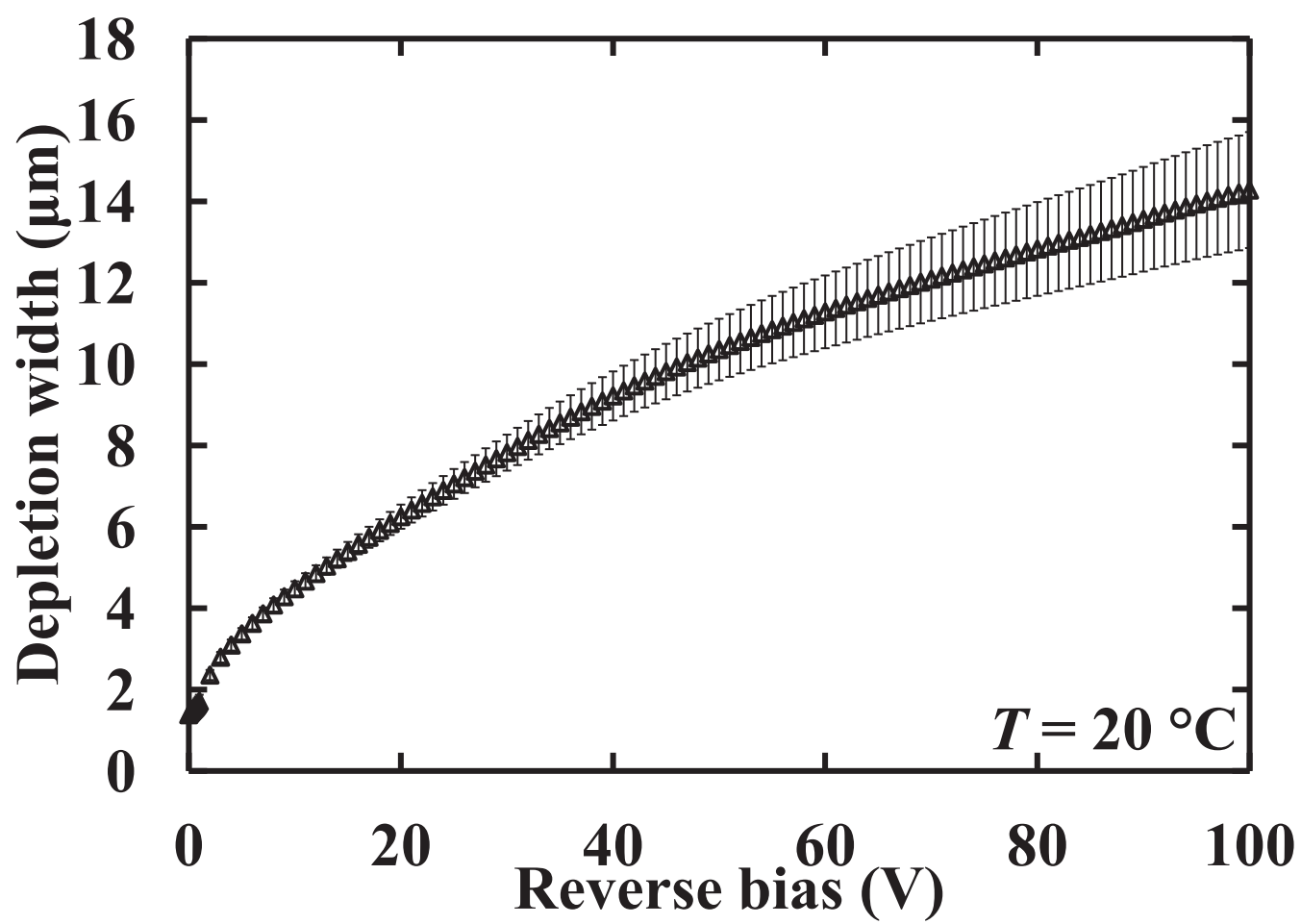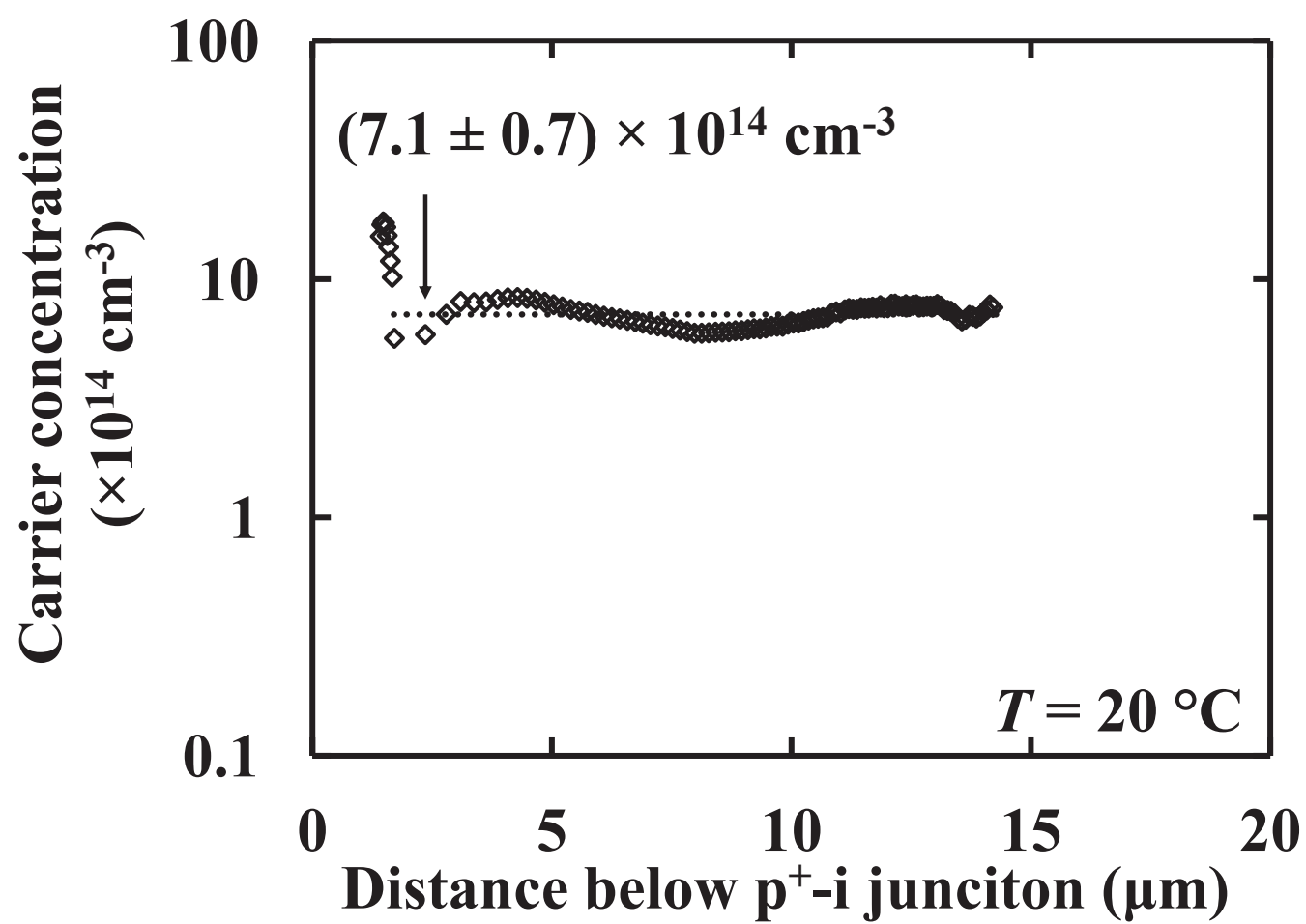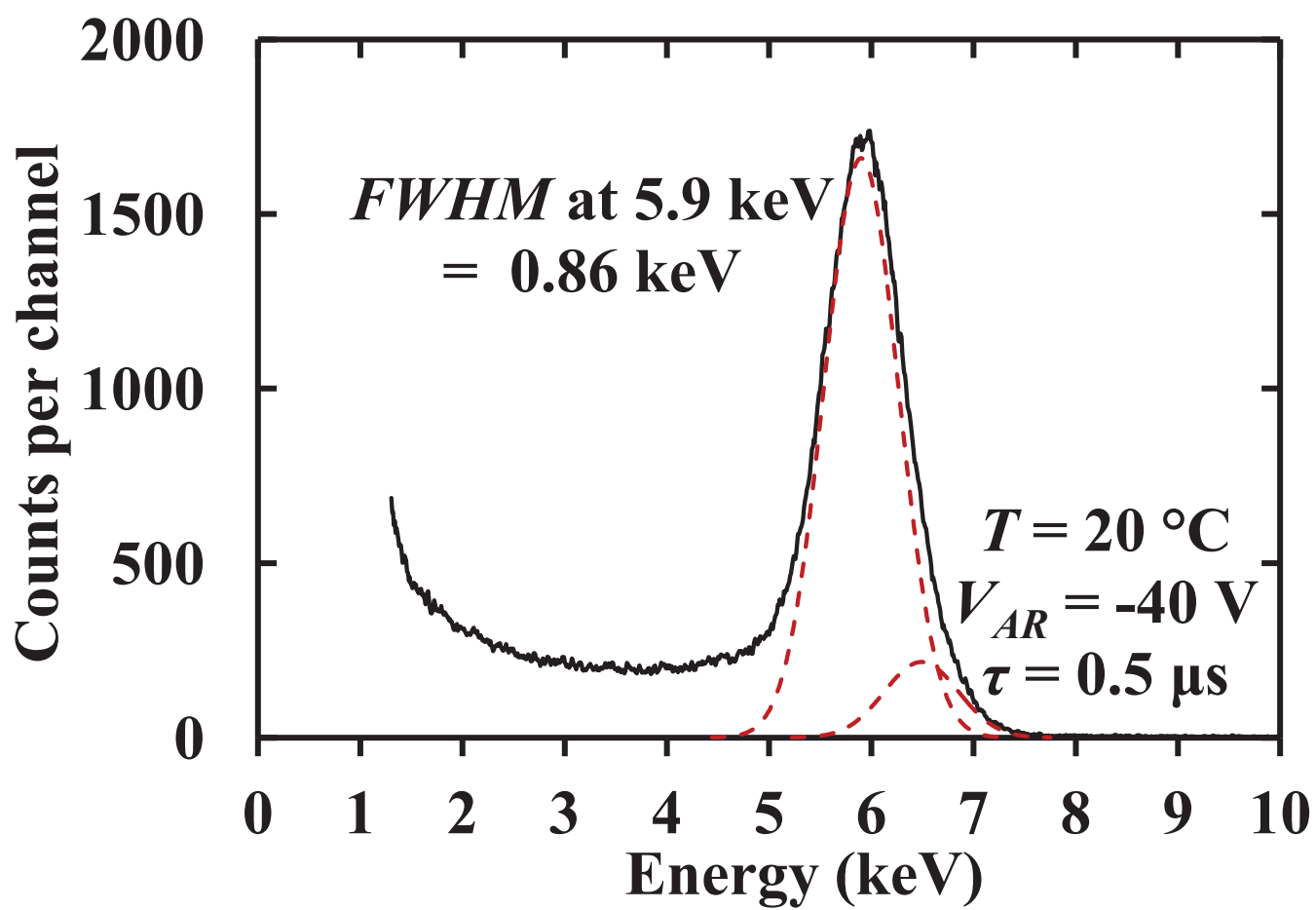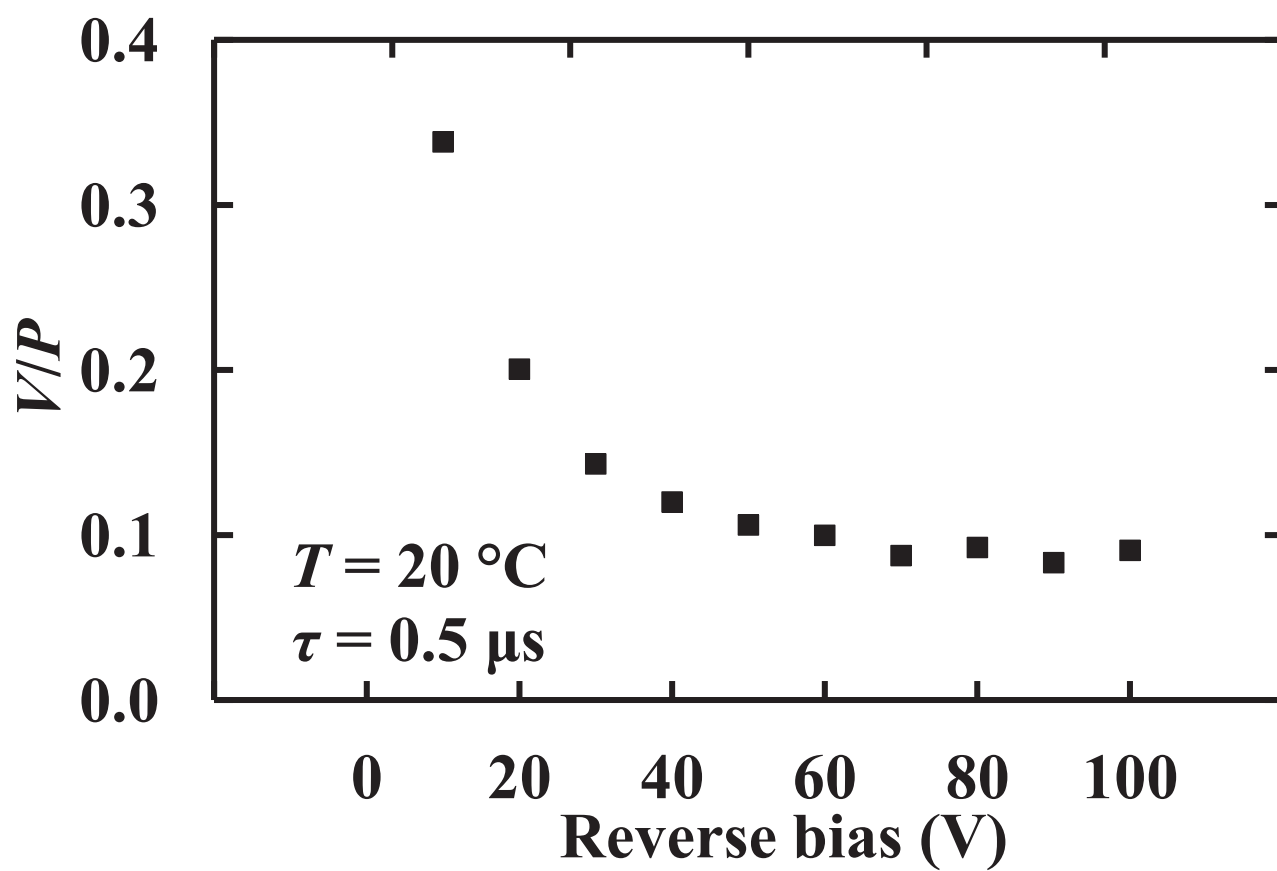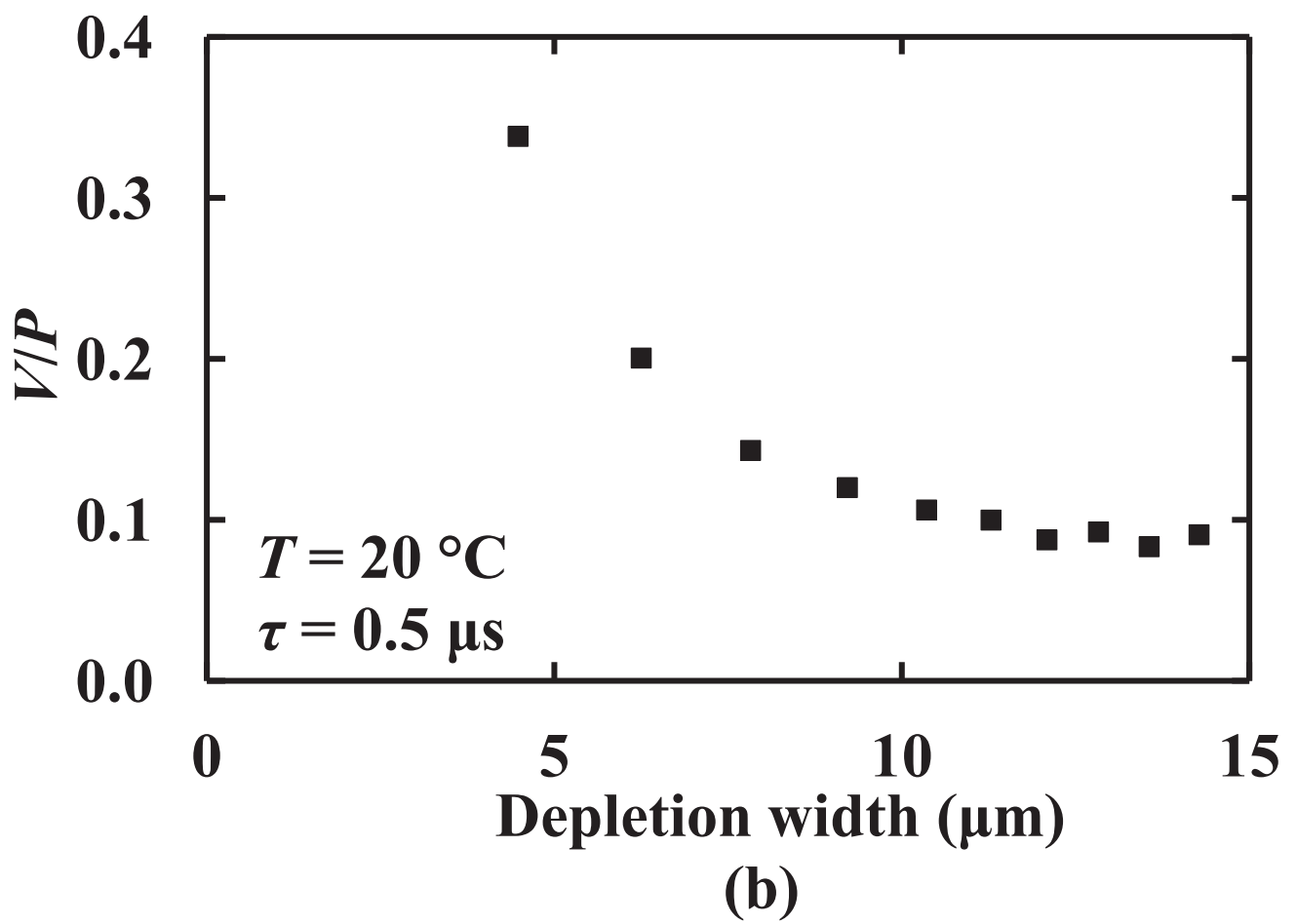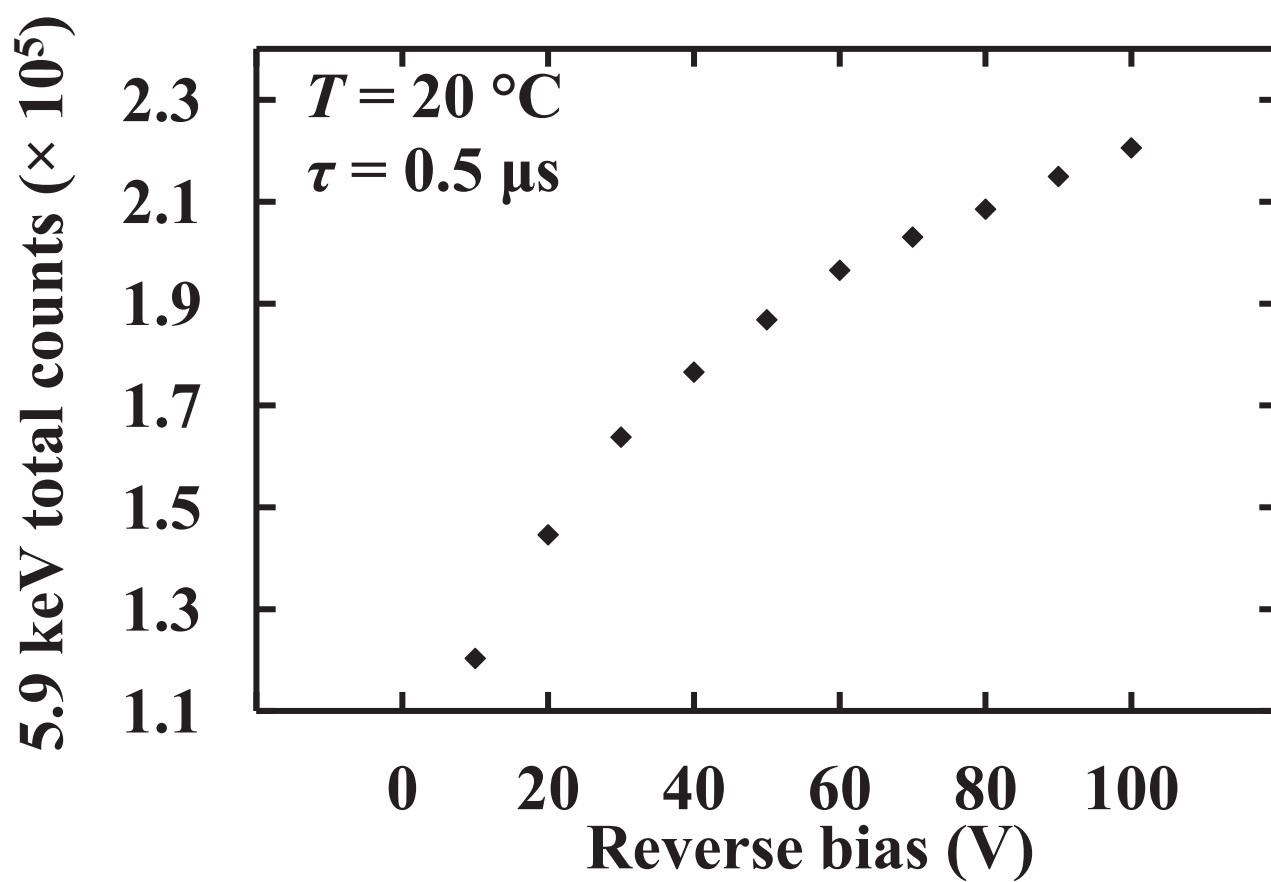
(b)
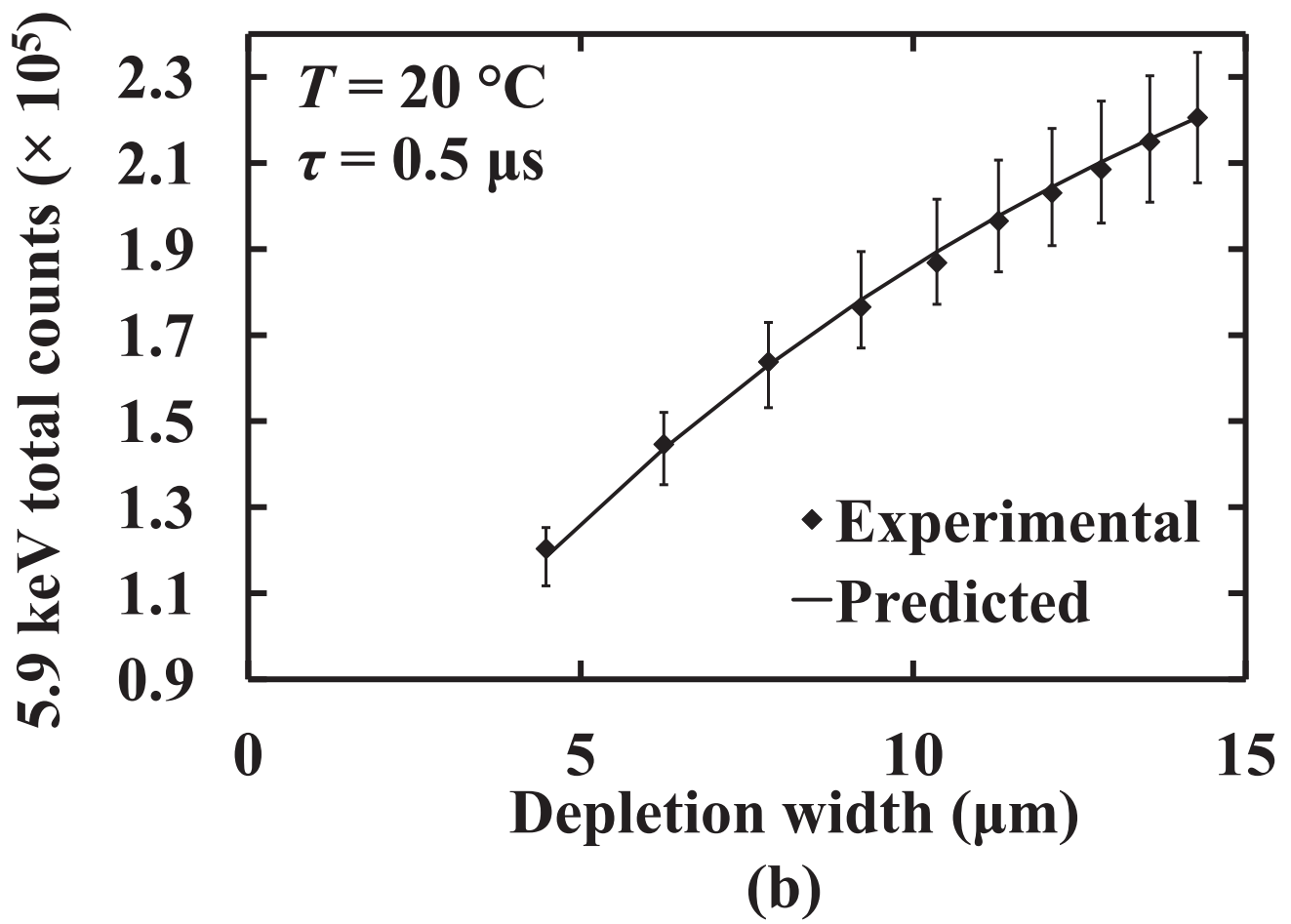
Figure 12

Figure 13

(a)
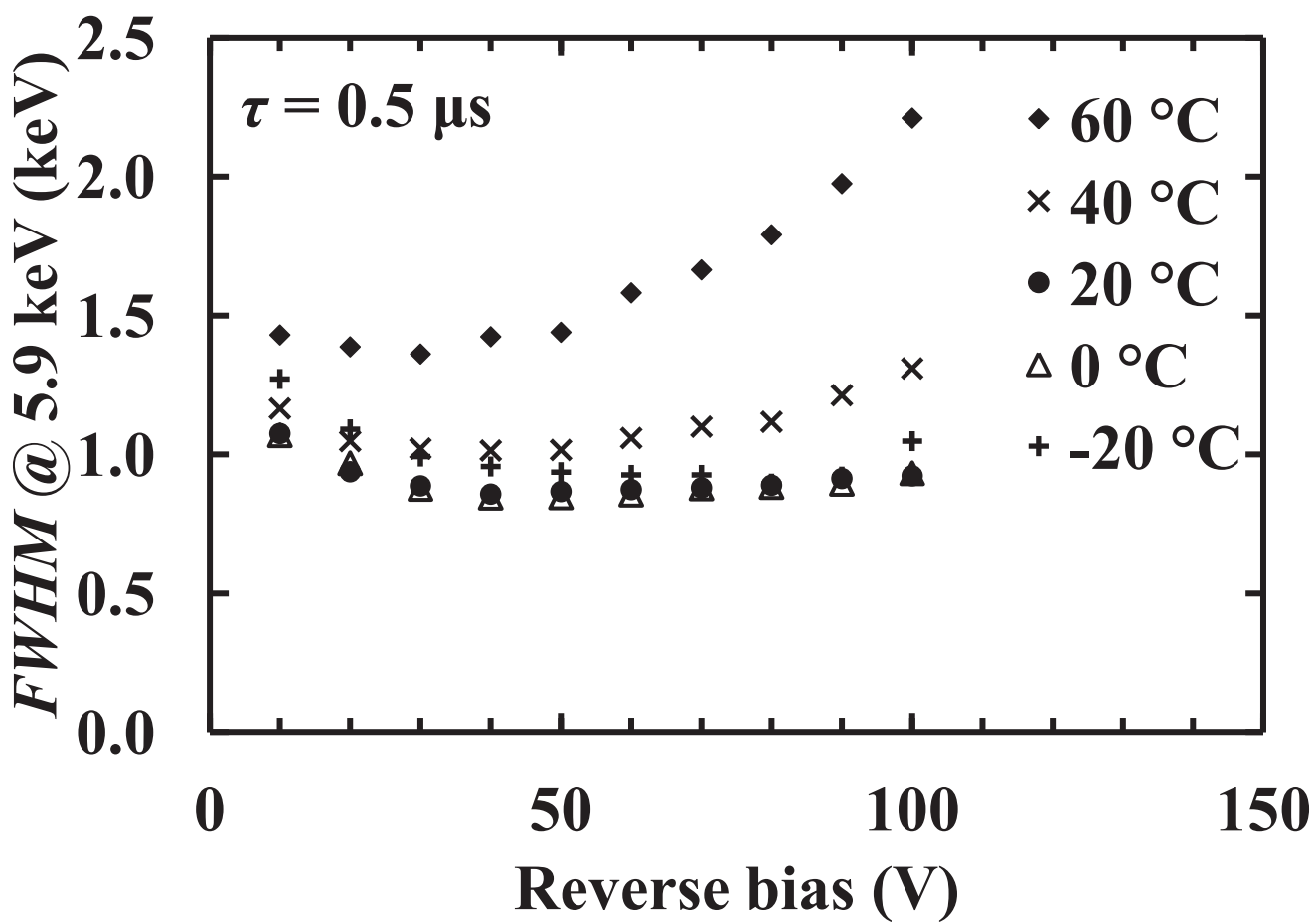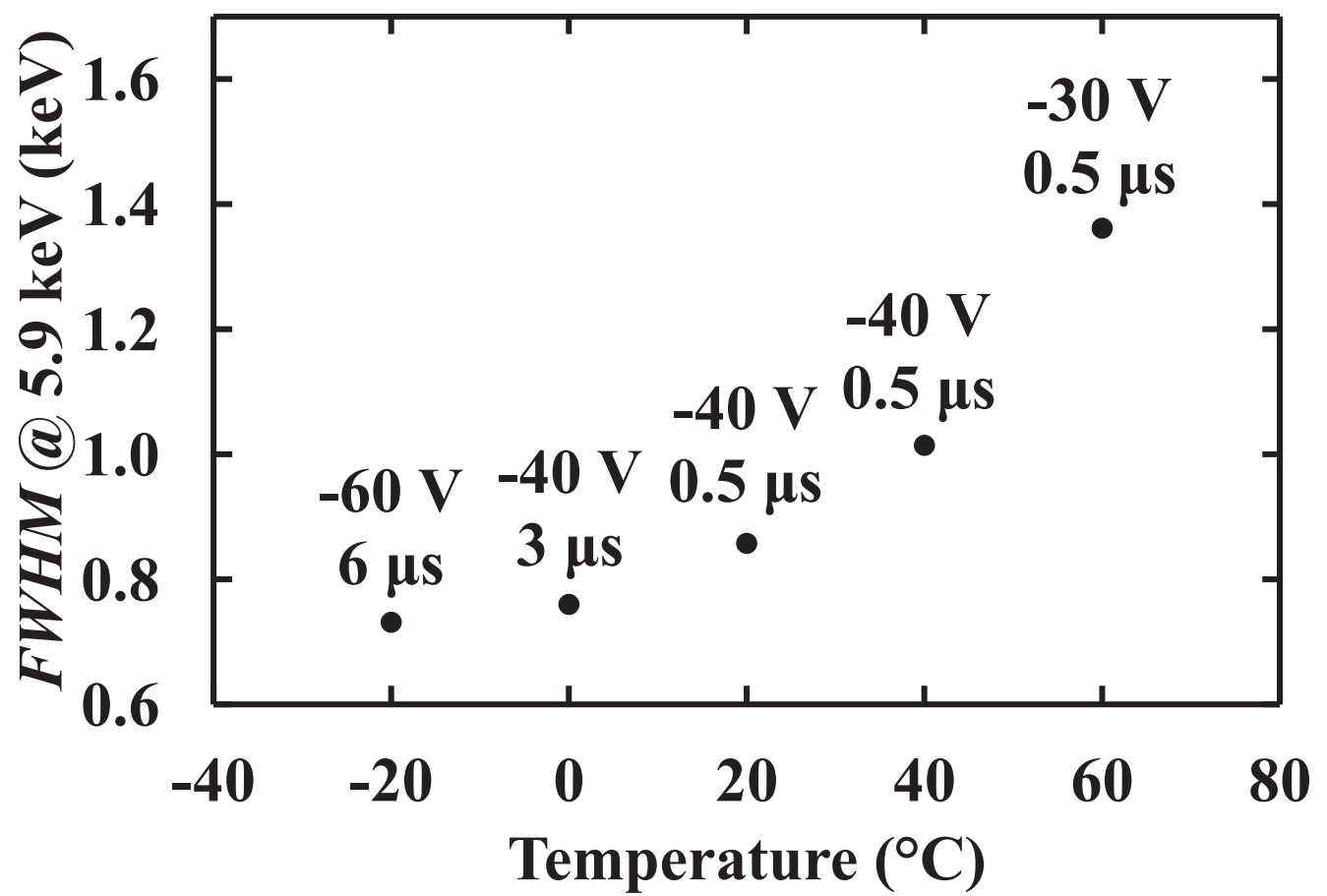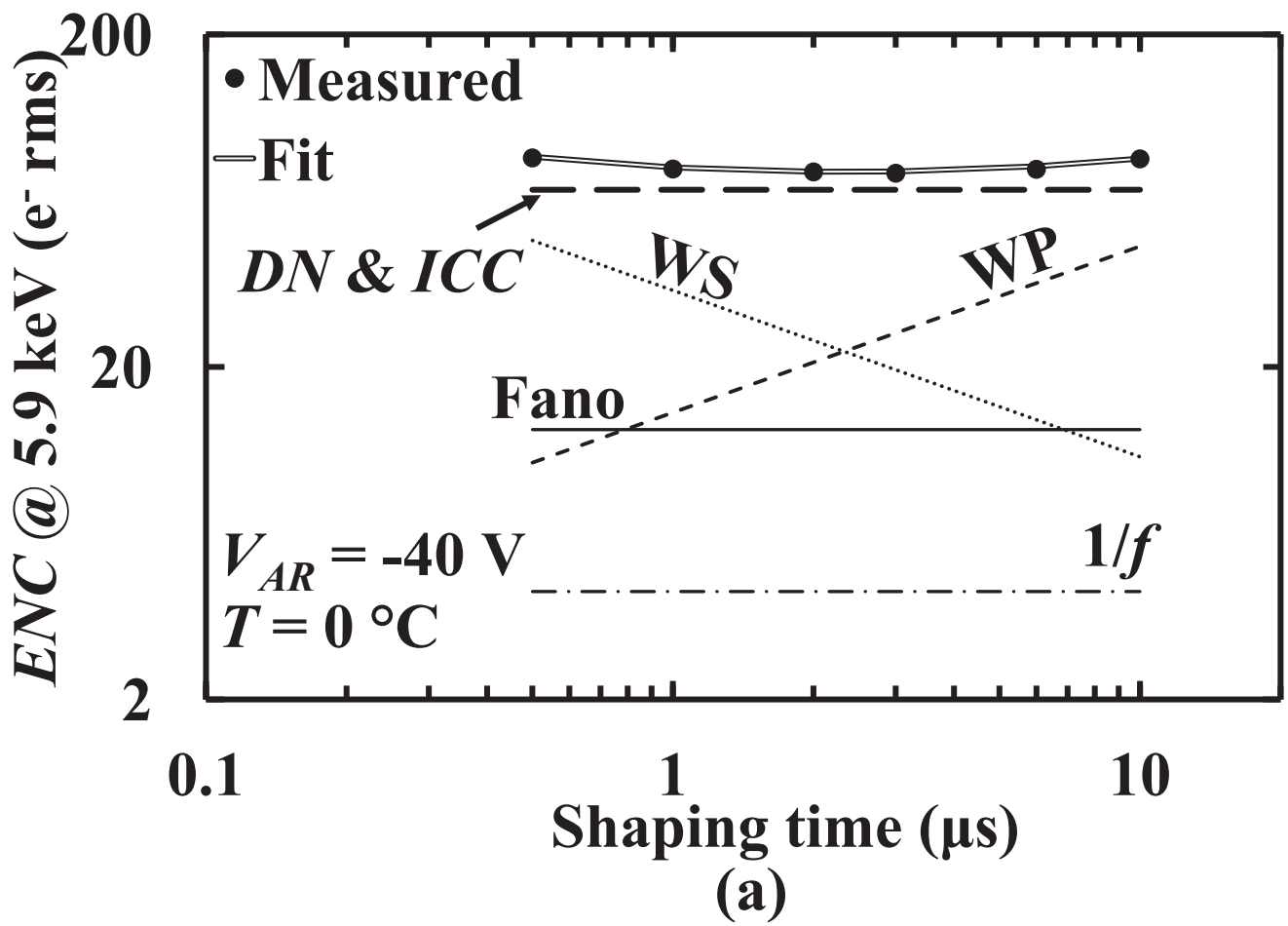
(b)
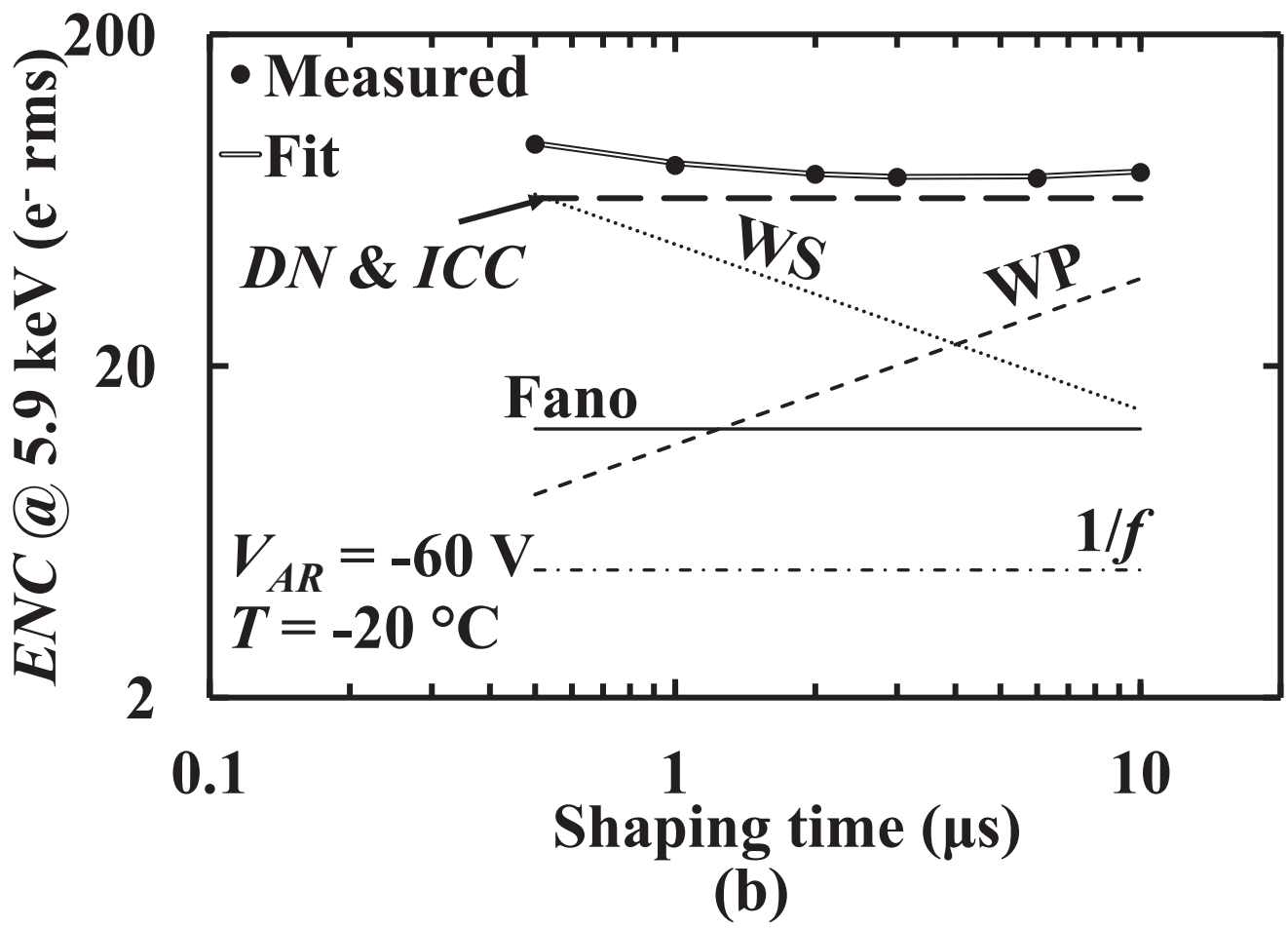
Table 1

Material	Type	Thickness (μm)	Doping density (cm^{-3})
GaAs	p$^+$	0.01	1×10^{19}
GaAs	p$^+$	0.5	2×10^{18}
GaAs	i	30	Undoped
GaAs	n$^+$	1	2×10^{18}
GaAs	n$^+$ (substrate)		